Hercynian anatexis in the envelope of the Beni Bousera peridotites (Alboran Domain, Morocco): Implications for the tectono-metamorphic evolution of the deep crustal roots of the Mediterranean region

Federico Rossetti [a,*], Federico Lucci [a], Thomas Theye [b], Mohamed Bouybaouenne [c], Axel Gerdes [d,e], Joachim Opitz [b], Andrea Dini [f], Christian Lipp [b]

[a] Dipartimento di Scienze, Università Roma Tre, Roma, Italy
[b] Institut für Anorganische Chemie, Universität Stuttgart, Stuttgart, Germany
[c] Département de Géologie, Université de Rabat, Rabat, Morocco
[d] Institute für Geowissenschaften, Goethe University, Frankfurt, Germany
[e] Frankfurt Isotope and Element Research Center (FIERCE), Goethe University Frankfurt, Germany
[f] Istituto di Geoscienze e Georisorse, CNR, Pisa, Italy

* Corresponding author at: Dipartimento di Scienze, Sez. Scienze Geologiche, Largo San Leonardo Murialdo, 1, 010146 Roma, Italy.
E-mail address: federico.rossetti@uniroma3.it (F. Rossetti).
https://doi.org/10.1016/j.gr.2020.01.020

a r t i c l e i n f o
Article history:
Received 29 October 2019
Received in revised form 13 January 2020
Accepted 29 January 2020
Available online 10 March 2020
Handling Editor: T. Gerya

a b s t r a c t
The metamorphic core of the Betic-Rif orogenic chain (Alboran Domain) is made up of lower crustal rocks forming the envelope of the Ronda (Spain) and Beni Bousera (Morocco) peridotites. The deepest sections of the crustal envelopes are made of migmatitic granulites associated with diffuse acidic magmatic products, making these exposure and ideal site to investigate the textural and petrological connection between crustal anatexis and granite magmatism in the contintental crust. However, still debated is the timing of intracrustal emplacement of the peridotite bodies, with models proposing either Alpine (early Miocene) or Hercynian ages, and still uncertain is the linkage between peridotite emplacement and crustal anatexis. In this study, by combining rock textures with whole-rock geochemistry, metamorphic thermobarometry, the U-Pb zircon geochronology and the analysis of the garnet and zircon REE chemistry, we document the P-T-t evolution of the granulite facies migmatites that form the immediate envelope of the Beni Bousera peridotites of the Rif belt. A main episode of Permo-Carboniferous (ca. 300–290 Ma) deep crustal anatexis, melt extraction and migration is documented thatwe link to the crustal emplacement of the Beni Bousera peridotites during collapse of the Hercynian orogen. Correlation at a regional scale suggests that the Beni-Bousera section can be tentatively correlated with the pre-Alpine (Permo-Carboniferous) basement units tectonically interleaved within the orogenic structure of the Alpine chain. The results of this study provide ultimate constraints to reconstruct the tectono-metamorphic evolution of the Alboran Domain in the Western Mediterranean and impose re-assessment of the modes and rates through which Alpine orogenic construction and collapse occurred and operated in the region.
Keywords:
Granulite
Anatexis
Hercynian
Alboran Domain
Western Mediterranean

1. Introduction

The arcuate belt of the Betic-Rif chain forms the western termination of the peri-Mediterranean Alpine orogenic systems (Fig. 1a). This orogen is part of a mountain belt developed along the active margin of the western Mediterranean subduction zone, developed during the Alpine Mesozoic-Cenozoic convergence between African and Eurasian plates (Dewey et al., 1989; Faccenna et al., 2001, 2004; Jolivet et al., 2008; Lonergan and White, 1997; Platt et al., 2013; Royden, 1993; Vérges and Fernàndez, 2012; Guerrera et al., 2019). The metamorphic core of this Alpine orogen is now dismembered in discontinuous outcrops located in the internal domains of the mountain fronts, where Neogene extensional tectonics overprinted the early crustal thickening event (e.g., Booth-Rea et al., 2007; Comas et al., 1999; Dewey, 1988; Faccenna et al., 2001, 2004; García-Dueñas et al., 1992; Jolivet and Faccenna, 2000; Jolivet et al., 2008; Michard et al., 2006; Platt and Vissers, 1989; Platt and Whitehouse, 1999; Platt et al., 1998, 2003a, 2003b, 2013; Guerrera et al., 2019; Van Hinsbergen et al., 2014).
The orogenic hinterland of the Betic-Rif chains consists of the continental-derived metamorphic units of the Alboran Domain (e.g., Andrieux et al., 1971; Casciello et al., 2015; Michard et al., 2006; Platt et al., 2013). Various models have been proposed in the literature with contrasting geodynamic and timing scenarios to frame the tectono-metamorphic evolution of the Alboran Domain. The major and Beni Bousera peridotite massifs (Fig. 1b). A distinctive feature of the Alpujarride/Sebtide Complex of the Alboran Domain is the presence of condensed metamorphic sequences with marked downward increase in the paleo-temperature gradients (Álvarez-Valero et al., 2014; Argles et al., 1999; Azañón et al., 1997; Balanyá et al., 1997; Barich et al., 2014; Booth-Rea et al., 2007; Comas et al., 1999; García-Casco

and Torres-Roldán, 1999; García-Dueñas et al., 1992; Gueydan et al., 2015; Haissen et al., 2004; Jolivet et al., 2008; Michard et al., 2006; Monié et al., 1994; Negro et al., 2006; Platt et al., 2013; Rossetti et al., 2005; Sánchez-Navas et al., 2014, 2017; Soto and Platt, 1999; Tubía et al., 1997; Zeck et al., 1992). Still debated is, in particular, the timing of the high-grade metamorphism and associated crustal anatexis in the metamorphic rocks that make-up the inner envelopes of the peridotite bodies, with implications on the age and model of the intracrustal emplacement of the peridotites. Based on the available petrological, structural and geochronological data sets, two classes of models exist, with the high-grade metamorphism and magmatism referred either to the Alpine (Álvarez-Valero et al., 2014; Argles et al., 1999; Esteban et al., 2004a, 2004b, 2010; Frasca et al., 2017; Garrido et al., 2011; Gueydan et al., 2015, 2019; Hidas et al., 2013; Homonnay et al., 2018; Janots et al., 2006; Mazzoli and Martín-Algarra, 2011; Précigout et al., 2013; Platt and Vissers, 1989; Platt et al., 1998, 2003a, 2003b; Platt and Whitehouse, 1999; Sánchez-Rodrıguez and Gebauer, 2000; Soto and Platt, 1999; Tubía et al., 1997; Whitehouse and Platt, 2003; Zeck et al., 1992) or the Hercynian (Acosta-Vigil et al., 2014; Barich et al., 2014; Bouybaouene et al., 1998; Michard et al., 1997; Montel et al., 2000; Rossetti et al., 2010, 2013; Ruiz Cruz and Sanz de Galdeano, 2014; Sánchez-Navas et al., 2014; Zeck and Williams, 2001; Zeck and Whitehouse, 1999, 2002) evolution. It is worth noting that disequilibrium textures and disturbance of the isotopic systems are also reported fromthe high-grade basement rocks of the Alboran Domain, suggesting a polyphase (Hercynian and Alpine) tectono-metamorphic evolution (e.g., Acosta-Vigil et al., 2014; García-Casco and Torres-Roldán, 1999; Gueydan et al., 2015; Massonne, 2014; Rossetti et al., 2010; Sánchez-Navas et al., 2017¸ Gómez-Pugnaire et al., 2019). Therefore, unanswered key questions regarding the tectono-thermal evolution of the Alboran Domain remain; in particular: (i) the age of crustal anatexis: Alpine or Hercynian?; (ii) which the link between crustal anatexis and the peridotite emplacement in the continental crust (time and mode of crust mantle coupling)?; and (iii) any correlations with the pre-Alpine lower crustal exposures across the Alpine chain (e.g., Schmid et al., 2004; von Raumer et al., 2013; Kunz et al., 2018)? To answer to these questions it is essential to elucidate the space-time connection (if any) between the partially molten source region (migmatites) and the extracted and migrated melts in the crustal section of the Alboran Domain, i.e. the so-called granulite–granite connection (e.g., Brown, 1994, 2013; Vanderhaeghe, 1999, 2009; Vielzeuf et al., 1990).

In this paper, we investigate the Pressure-Temperature-time (P-T-t) evolution of the granulite facies migmatites (kinzigites in Kornprobst, 1974) that form the immediate envelope of the Beni Bousera peridotite at the core of the Alboran Domain of the Rif belt (Figs. 1b and 2). We report a main Permo-Carboniferous deep crustal granulite-granite suite that we link to the crustal emplacement of the Beni Bousera peridotites and discuss implications of these results for the tectono-metamorphic evolution of the Alboran Domain and of the Alpine orogen in general.

2. Geological setting

The Alboran Domain forms the metamorphic core of the Alpine Betic-Rif orogen. It consists of continentally-derived metamorphic rock units that broadly correlate across the two arms of the orogeny (García-Dueñas et al., 1992; Michard et al., 2006) (Fig. 1b).

In Morocco, the Alboran Domain is made of the Ghomaride and Sebtide complexes that tectonically overlie the Mesozoic carbonates of The Dorsale units (Figs. 1b and2). In the Betics, these metamorphic complexes correspond to the Malaguide and Alpujarride complexes, respectively. The lower tectonic complex is the eclogite-bearing Nevado-Filabride Complex (Augier et al., 2005; Puga et al., 1999) of the Betics

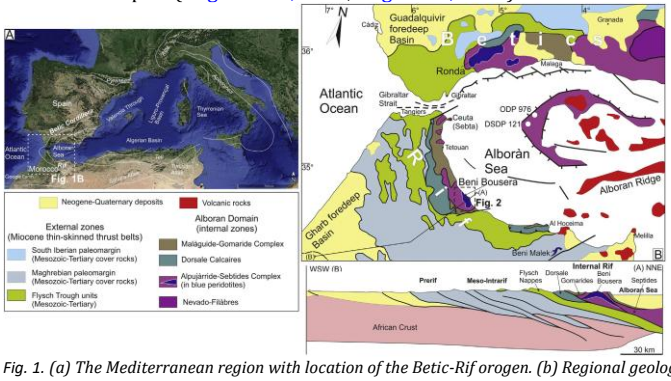

Fig. 1. (a) The Mediterranean region with location of the Betic-Rif orogen. (b) Regional geology of the western Mediterranean

region and crustal-scale geological cross section across the Rif chain (modified and re-adapted after Michard et al., 2006 and references therein). The study area (Fig. 2) is also indicated.

that is not exposed in theMoroccan side (Michard et al., 2006 and references therein) (Fig. 1b).

The metamorphic signature the Alpujarride-Septide complex has been classically referred to as a down-section transition from low-grade (subduction-type) to high-grade (Barrovian-type) thermo-baric environments, as recorded on Permian-Triassic and pre-Alpine protoliths, respectively (Azañón et al., 1997; Bouybaouene et al., 1998; ElMaz and Guiraud, 2001;Michard et al., 1997, 2006).The age of theAlpine subduction zone metamorphism is still poorly constrained but referred to as Eocene (Platt et al., 2005). In the Moroccan Rif, this distinct metamorphic signature corresponds to the upper (Federico Group) and lower (Filali and Beni Bousera units) Sebtides, respectively (Kornprobst, 1974; Michard et al., 2006; Bouybaouene et al., 1998; Negro et al., 2006; Gueydan et al., 2015) (see the tectono-stratigraphic column in Fig. 2a). This down-section change in the metamorphic signature is structurally Associated with the presence of large peridotite bodies (Ronda and Beni Bousera; Fig. 1b), which are tectonically interlayered within the continental metamorphic sequence of the Alpujarride-Septide complex.

Field evidence documents similar contact relationships between the peridotite bodies and the hosting continental-derived Alpujarride-Sebtides units (e.g., Michard et al., 2006). High-grade metamorphic rocks characterise the upper and lower contacts of the peridotites with widespread evidence of rock anatexis close to these contacts. The upper tectonostratigraphic section corresponds to the Casares-Los Reales unit of the Betics (Monié et al., 1994; Haissein et al., 2004) and to the Lower Sebtides of the Rif (Kornprobst, 1974; Michard et al., 2006), consisting of basal acidic migmatitic granulites (kinzigites and Beni Bousera units) passing upward to lower-grade gneisses and metapelites of the Filali unit. Peak metamorphism in the Casares-Los Reales/Beni Bousera units is commonly framed within the HP granulite facies field (1.2–1.7 GPa and 750–850 °C), typified by the assemblage garnet-kyanite-rutile ± biotite, followed by a nearly isothermal decompression within the cordierite stability field (Bouybaouene et al., 1998; Haissein et al., 2004; Álvarez-Valero et al., 2014).

The lower contact with the crustal envelope is well exposed in the western Betics, where the peridotites rest on top of the Blanca Group, a migmatitic, locally strongly mylonitised, inverse metamorphic sequence grading from granulite (top) to amphibolite (bottom) facies metamorphic conditions (Acosta-Vigil et al., 2014; Tubía et al., 1997; Torres-Roldán, 1983). In the Moroccan Rif, the basal contact is exposed in the Ceuta area (Fig. 1b), where the peridotite bodies tectonically rest on top of the Monte Hacho gneiss (Kornprobst, 1974; Homonnay et al., 2018; see tectono-stratigraphic column in Fig. 2a). The lower and upper contacts of the peridotites and the associated partial melting are interpreted as dynamothermal aureole developed during the intracrustal emplacement of the peridotites, and considered as developed during hot thrusting and extensional unroofing and decompression in Alpine times, respectively (e.g. Argles et al., 1999; Frasca et al., 2017; Gueydan et al., 2019; Hidas et al., 2013; Homonnay et al., 2018; Mazzoli and Martín-Algarra, 2011; Platt et al., 2003a, 2003b, 2013; Tubía and Cuevas, 1986; Tubía et al., 1997). Evidence of an early UHP evolution, assumed as Hercynian in age, has been also reported from the Jubrique zone of the Alpujarride Complex in the Betic Cordillera (Ruiz Cruz and Sanz de Galdeano, 2014) and from the orthogneiss of the Hacho unit in the Ceuta zone (Ruiz-Cruz and Sanz de Galdeano, 2012, 2013).

No definitive constraint on the granulite-granite connection issue has been derived since now in the Betic-Rif realm. The age of the anatectic products and melt mobilisates found within the immediate envelope of the peridotite bodies is still the subject of debate, with Alpine and Hercynian ages proposed so far (see Acosta-Vigil et al., 2014 for a recent review). Granite magmatism in the Ronda area (Betics) is commonly attributed to the early Miocene (Rb-Sr, whole-rock (Priem et al., 1979); Ar-Ar on biotite (Monié et al., 1994); U-Pb zircon dating

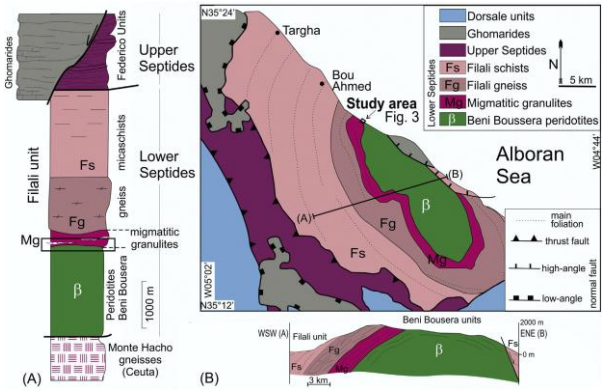

Fig. 2. (a) Tectono-stratigraphic column of the Alboran Domain Complex in the Moroccan Rif (modified and re-adapted after Michard et al., 1997), with indication of the migmatitic granulites (Mg) that are the focus of this study. (b) The geology of the study area (modified after Kronmpbost, 1974). (c) General structural architecture across the Beni Bousera peridotite bodies (geological cross-section A-B).

(Esteban et al., 2010)). However, magmatic rocks of Hercynian age are also reported from the Betic Cordillera (Priem et al., 1966; Platt and Whitehouse, 1999; Zeck and Williams, 2001). Recently, through SHRIMP U-Pb zircon geochronology, Sánchez-Navas et al. (2014) have documented Hercynian (286 ± 16 Ma) igneous zircons and Alpine metamorphic resetting (early Miocene in age) in granitoid dykes intruded in the Torrox unit of the Central Betics.

This duality of Hercynian and Alpine ages for the granitemagmatism is also documented in the immediate envelope of the Beni Bousera peridotites in the Rif (Fig. 1),where two generation of peraluminous granites with distinct isotopic signatures are recognised (Rossetti et al., 2010, 2013): (i) an early HP, garnet-kyanite-bearing, granitic suite with highly radiogenic Sr isotope ratios (0.736243–0.771449) (the socalled "leptinites" Kornprobst (1974) of Hercynian age (Permo-Carboniferous, 290–300 Ma; U-Pb zircon dating); and (ii) a subsequent LP, andalusite-bearing, sub-vertical granite dyke swarm with lower Sr radiogenic rations (0.719753–0.722461), dated by coupled U-Pb zircon/monazite and $^{40}Ar/^{39}Ar$ muscovite/biotite geochronology to the early Miocene (c. 22 Ma).

The Hercynian and Alpine ages are also systematically derived from the U-Th-Pb zircon and monazite geochronology of the migmatitic sequences of the Alboran Domain, where a significant inheritance from Cadomian-Pan African (560–640Ma), Grevillian (940–1020Ma), to Archean (2–2.5 Ga) crustal sources are also reported (Zeck andWilliams, 2001; Platt and Whitehouse, 1999; Zeck and Whitehouse, 1999, 2002; Acosta-Vigil et al., 2014; Montel et al., 2000; Rossetti et al., 2010; Sánchez-Navas et al., 2014; Melchiorre et al., 2017).

Based on U-Pb SHRIMP dating on structureless zircon rims from both the migmatitic dynamothermal sole and syn-tectonic intrusives from the Blanca unit of Central Betics, Esteban et al. (2010) proposed an age of 22–21 Ma for the intracrustal emplacement of the Ronda peridotites. Similarly, U-Pb zircon and Ar-Ar datings of syn-tectonic and post-tectonic intrusive granitic dykes constrain the crust-mantle coupling in the Ronda area during the Early Miocene (22.5–20 Ma; Frasca et al., 2017). However, based on integrated petrographic/textural and SHRIMP U-Pb dating of magmatic zircons, Acosta-Vigil et al. (2014) have constrained the age of anatexis at the footwall of the Ronda peridotite to the late stages of the Hercynian orogeny (280–290Ma), and documented an Alpine-aged recrystallisation and Pb loss event in the Hercynian zircons. These Hercynian ages are in line with the U-Pb zircon dating results derived from (i) the migmatitic portions of the Torrox basement units, which provided mean ages of 285 ± 5 Ma, 313 ± 7 Ma (Zeck and Whitehouse, 2002) and 286 ± 11 Ma (Sánchez-Navas et al., 2017), and (ii) the migmatitic sequences of the Jubrique zone (mean ages of 330 ± 9 and 265 ± 4 Ma) (Ruiz Cruz and Sanz de Galdeano, 2014), both structurally overlying the Ronda peridotites.

Regarding the high-grade migmatitic crustal envelope of the Beni Bousera peridotites, Montel et al. (2000), have documented late Hercynian (284 ± 27 Ma) granulite metamorphism, as derived from U-Th-Pb dating of monazite inclusions in garnet. The intrusive relationships between Permo-Carboniferous granitoid bodies and the host Beni-Bousera units, allowed Rossetti et al. (2010) to propose a pre-Alpine age for the crustal envelope of the Beni Bousera peridotites. On the other hand, Platt et al. (2003a) provided a lower Miocene (22.7 ± 0.3 Ma) U-Pb zircon age for the peak of metamorphism in the Beni Bousera

units that is referred to as the main stage of crustal thinning and exhumation. Finally, Melchiorre et al. (2017) reported new zircon U-Pb ages from the Beni Bousera granulites, which provided ages spanning from Paleoproterozoic (1508±23Ma) to Miocene (22.9±0.7Ma). In particular, two main groups of ages at ca. 286–264 and ca. 23 Ma are derived, interpreted as the timing of the prograde HP metamorphism and the LT exhumation of the granulite envelope, respectively (Melchiorre et al., 2017).

As a final point, it is worth noting that the early Miocene granite magmatism overlaps in time with the wealth of the available radiometric geochronological and low-temperature thermochronological data (apatite and zircon fission tracks) from the Sebtide-Alpujarride realm that, regardless of the dating method, indicates a significant age clustering at 18–25 Ma, commonly interpreted as the time of cooling and exhumation of the Alboran Domain (e.g., Michard et al., 2006; Janots et al., 2007; Frasca et al., 2017; Gueydan et al., 2015; Homonnay et al., 2018; Melchiorre et al., 2017; Monié et al., 1994; Platt et al., 1998, 2003b; Platt and Whitehouse, 1999; Rossetti et al., 2010; Sánchez-Rodrıguez and Gebauer, 2000; Zeck et al., 1992; Azdimousa et al., 2014; Sosson et al., 1998; Esteban et al., 2004a, 2004b, 2007; 2011; Andriessen and Zeck, 1996).

3. The study area

The study area corresponds to the north-western, high-grade envelope of the Beni Bousera peridotites, where the lower Sebtides are exposed. The lithological units grade from granulite migmatites (kinzigites) at the contact with the peridotite (collectively named as the Beni Bousera units) to gneisses and micaschists of the Filali unit (Fig. 2a,b). The regional metamorphic foliation wraps around the Beni Bousera peridotites, showing a general domal attitude (Álvarez-Valero et al., 2014; Bouybaouene et al., 1998; El Maz and Guiraud, 2001; Gueydan et al., 2015; Kornprobst, 1974; Melchiorre et al., 2017; Michard et al., 2006; Negro et al., 2006) (Fig. 2b,c). As documented by Raman spectroscopic analyses of graphitic material from the Filali unit (Negro et al., 2006), the metamorphic grade increases down-section from subsolidus andalusite to kyanite zones, with melting occurring at the transition from the Filali mica schists to the Filali gneiss in correspondence of the sillimanite + alkali feldspar isograd (El Maz and Guiraud, 2001). The metamorphic signature of the Filali unit is described as acquired during a polyphase clockwise P-T path in response to a transition from a Hercynian Barrovian stage (peak conditions of 550–670 °C and 0.5–08 GPa) metamorphic gradient of 20–26 °C/km), followed and overprinted by a HT-LP one (equilibrated at 550–750 °C and 0.3–06 GPa; metamorphic gradient of 45 °C/km), Alpine in age (at ca. 21 Ma; Gueydan et al., 2015).

The granulite envelope is dominantly made of felsic (metapelite-derived) and minor mafic protoliths, the latter occurring as intercalations and boudins close to the contact with the peridotites (Bouybaouene et al., 1998; Haissen et al., 2004; Álvarez-Valero et al., 2014; Melchiorre et al., 2014). The thermobaric evolution of the granulite rocks is similarly framed within a nearly isothermal decompressional evolution, starting at HP/HT conditions of 1.2–1.5 GPa (up to 2.0 GPa in the basic granulites; Bouybaouene et al., 1998) at ca. 800 °C, with a final re-equilibration at 0.4–0.5 GPa for T below ca. 600 °C (Bouybaouene et al., 1998; Haissein et al., 2004; Álvarez-Valero et al., 2014). Age of the climax of metamorphism is still debated, referred either to the Hercynian (Michard et al., 1997; Bouybaouene et al., 1998; Montel et al., 2000; Rossetti et al., 2010; Melchiorre et al., 2017) or the Alpine (Early Miocene; Platt et al., 2003a, 2003b; Gueydan et al., 2015) tectono-metamorphic evolution. Available zircon and apatite zircon fission-track data constrain the final exhumation of the Beni Bousera peridotite massif during Burdigalian-Langhian times (ca. 19.5–15.5 Ma; Azdimousa et al., 2014).

4. Materials and methods

This study investigates a suite of migmatitic granulites in the immediate envelope of the Beni Boussera peridotites, exposed on a ca. 500 m long, continuous outcrop (known as Playa Smeila) located along the sea side, 1 kmsouth-east of the Bouh Ahmed village (Figs. 2band3a). Meso- and micro-scale studies were carried out in order to investigate the petrology and geochronology of rock anatexis and melt formation.

Selected rock samples, representative of the different textures recognised in the field, were chosen for petrographical investigation, mineral and whole-rock chemistry (major and trace elements). Sample selection was based on the structure at the outcrop scale and on meso-

and micro-scale textural and mineralogical features. Samples are shown in their structural context in Fig. 3a and listed in Table 1, where their location, fabrics, and constituent mineralogy are detailed. Electron microprobe analyses (EMPA) were used to define compositions of the constituent mineral assemblages. Inverse and forward modelling techniques (Powell and Holland, 2008) were used to assess the thermobaric conditions associated with anatexis, magma segregation and emplacement. The U-(Th)-Pb zircon geochronology was adopted to

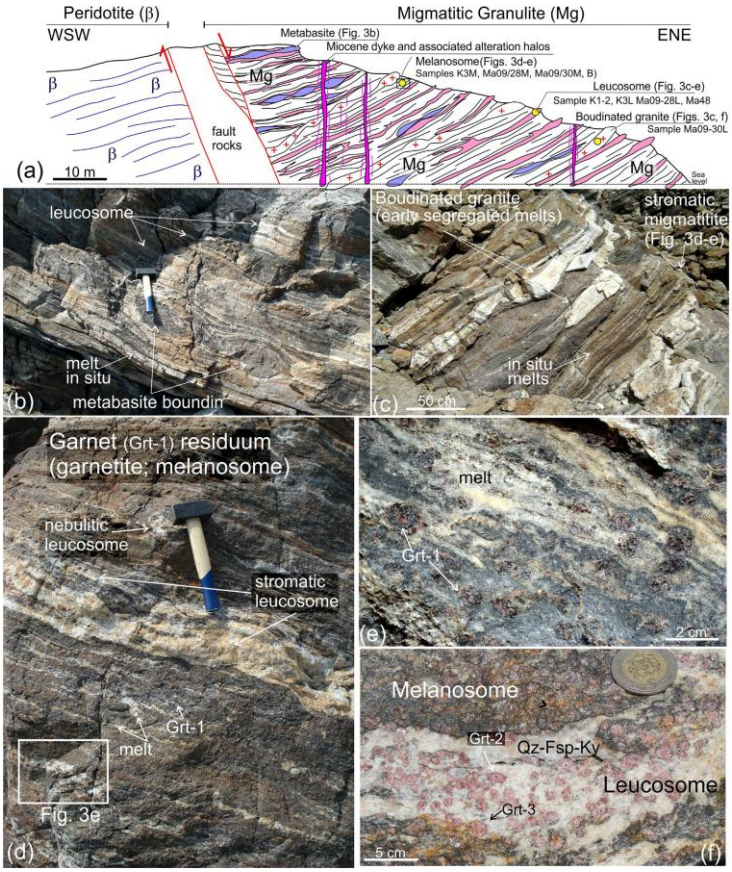

Fig. 3. Outcrop-scale rock textures in the field. (a) Geological sketch showing the across-strike structure of the peridotite (ß)-migmatitic granulites (Mg) contact (Beni Bousera units), showing representative lithologies and the structural significance of the studied samples (see also Table 1). (b) Stromatic leucosome layering within the granulites enveloping metabasite boudins. (c) Coexistence of deformed (early segregated) leucosomes and stromatic leucosome layering within the granulite foliation. (d) Coarse-grained garnet-bearing (Grt-1) residua (melanosome) hosting stromatic and nebulitic leucosomes (stromatic metatexite). (e) Detail shown in (d) showing the intimate relationships between garnet (Grt-1) and leucosomes. (f) The melanosome-leucosome contact showing enclaves of grt-bearing melanosome portions and the two igneous garnet types (Grt-2 and Grt-3, sample). Mineral abreviations follow Whitney and Evans (2010).

constrain the timing of crustal anatexis and magmatism in the metamorphic envelope. Trace and rare earth element (REE) compositions (both in situ and on separates) of zircon and garnet were also investigated to link the U-Pb zircon ages to the reconstructed tectonometamorphic history.

Details on the analytical methods and protocols adopted in this study are provided in the Supplementary Material 1. In the following, mineral abbreviations are after Whitney and Evans (2010).

5. Structure and petrography of the granulites

The granulites are characterized by a north-eastward dipping foliation that is sub-parallel to the one in the underlying peridotites. A major, NW-SE steeply-dipping extensional fault, marked by a ca. 20 wide damage zone, cuts across the granulite-peridotite contact. The whole outcrop is affected by intense jointing that defines NW-SE striking sub-vertical fracture arrays associated with rock alteration in both the footwall and hangingwall rocks. A subparallel pegmatitic dyke swarm is observed to intrude the granulite rocks (Fig. 3a).

The granulites are extensively migmatitic, with an overall stromatic texture, made of centimetre- to decimetre-scale lithological banding parallel to the dominant foliation at the outcrop scale, and defined by alternating leucocratic and melanocratic portions (Fig. 3b–e). The granulites host dm-scale metabasite boundins, typically surrounded by

leucocratic layers and lenses, and with boudin necks providing dilatational sites for accumulation of leucocratic material (Fig. 3b). Following Sawyer (2008), the leucocratic portions consist of both in situ and insource leucosome types (up to 30–40% vol.), associated with leucocratic sills (up to 10% vol.) (Fig. 3a–e). The latter are typically extensively boundinaged and stretched along the main foliation (Fig. 3c). The melt structures (leucosomes and sills) invariably contain high proportions of garnet. The melanocratic portions are here almost entirely constituted by mm to cm-thick porphyroblastic aggregates of garnet and interpreted as a melt residuum (Taylor and Stevens, 2010). In particular, garnet porphyroblasts (up to 3 cm in diameter) are surrounded by and embedded within diffuse leucocratic patches and layers (Fig. 3d,e), suggestive of in situ melting, likely developed through incongruent melting reactions in which the garnets are formed as the solid peritectic products (e,g,. Brown, 2013). Based on the overall rock texture, the Beni Bousera granulites can be classified as a metatexite migmatite (e.g., Brown, 1994; Sawyer, 1994).

The rock mineralogy is dominated by modally abundant Grt (locally up to 60 vol%) in an igneous matrix made of Qz-Pl-Kfsp-Ky+Gr, Rt (see Supplementary Material 2 for representative EMPA of the mineral constituents). Accessories include Zrn, Ap, and Mnz. The igneous assemblage in the melt segregates (leucosomes and sills) resembles peraluminous granites (e.g. Clarke, 1981) (Figs. 3d–f and 4). Three main generations of garnets can be recognised based on textural evidence, with distinct inclusion assemblages and composition zoning (see below). An early garnet generation (Grt-1), occurring primarily in the melanosome portions, consists of coarse-grained (up to 1–3 cmin diameter), anhedral grains, usually with distinct core and rim structures. The inner Grt-1 cores are typically devoid of mineral inclusion, whereas the outer core and rim domains are poikilitic, hosting numerous (10–200 μm) xenomorphic and round to lobate mono- and poly-mineralic inclusions typically made of Qz-Kfs ($Ab_{13–17}$)-Pl ($An_{35–45}$) aggregates, usually associated with Rt, Gr and Bt with high TiO_2 (up to 7.76 wt%) and high X_{Mg} ([Mg/(Mg + Fe)]×100) = 51–60). Significantly, the outer core domains are also characterized by dense arrays of graphite-bearing fluid and solid inclusions, where usually Ky occurs embayed in multiphase Pl-Kfs-Qz aggregates (Fig. 4a–d). The presence of Sill inclusions is instead systematically observed in the rim domains of the largest Grt-1 grains (Fig. 4e). A second generation (Grt-2), occurring in leucosomes, consists of large (up to 1–2 cm in diameter), still poikilitic and anhedral grains hosting Qz-Kfs-Pl

Table 1 - Location of analysed samples with constituent mineralogy and analytical techniques

Sample	Latitude	Longitude	Rock type	Mineral assemblage	EMPA	U-(Th)-Pb geochronology	whole rock geochemistry	in situ LA-ICPMS analysis
K3M	N35°19'19.6"	W004°55'51.2"	Melanosome	Qz-Kfs-Pl-Gt-Bt-Ky/Sil-Rt +Crd +Ap +Zrc +Mnz	X		X	
K3L	N35°19'19.6"	W004°55'51.2"	Leucosome	Qz-Kfs-Pl-Gt-Bt-Ky-Rt +Sil +Ap +Zrc	X	X	X	X
K1	N35°19'19.6"	W004°55'51.2"	Leucosome	Qz-Kfs-Pl-Gt-Bt-Ky-Rt +Sil +Ap +Zrc	X		X	
K2	N35°19'19.6"	W004°55'51.2"	Leucosome	Qz-Kfs-Pl-Gt-Bt-Ky/Sil-Rt +Sil +Ap +Zrc	X		X	
Ma09/28M	N35°19'19.6"	W004°55'51.2"	Melanosome/Leucosome layering	Qz-Kfs-Pl-Gt-Bt-Ky/Sil-Rt +Crd + Ap + Zrc +Mnz	X		X	
Ma09/28L	N35°19'19.6"	W004°55'51.2"	Leucosome	Qz-Kfs-Pl-Gt-Bt-Ky-Rt +Sil +Ap +Zrc		X	X	X
B	N35°19'20.1"	W004°55'41.8"	Melanosome/Leucosome layering	Qz-Kfs-Pl-Gt-Bt-Ky/Sil-Rt +Crd + Ap + Zrc +Mnz	X		X	
Ma09/30L	N35°19'20.1"	W004°55'41.8"	Leucosome	Qz-Kfs-Pl-Gt-Bt-Ky-Rt +Sil +Ap +Zrc	X	X	X	X
Ma09/30M	N35°19'20.1"	W004°55'41.8"	Melanosome/Leucosome layering	Qz-Kfs-Pl-Gt-Bt-Ky/Sil-Rt +Crd + Ap + Zrc +Mnz	X		X	
Ma48	N35°19'20.1"	W004°55'41.8"	Melanosome/Leucosome layering	Qz-Kfs-Pl-Gt-Bt-Ky/Sil-Rt +Crd + Ap + Zrc +Mnz	X			

inclusion assemblages, usually associated with Sil in the core domains (Fig. 4f). Ky crystals either as single mineral inclusion or associated with Pl-Kfs-Qz aggregates are commonly observed at the Grt-2 rims (Fig. 4g). The third garnet generation (Grt-3) occurs again only in the leucosomes and typically show anhedral grain shapes with a nearly uniform grain size (ca. 50–250 μm), interstitially distributed along Qz-Fsp grains boundaries, indicating that Grt-3 directly crystallised from a melt (Fig. 4h). Igneous textures are usually well preserved in the low strain domains, as documented by a well annealed polygonal texture made of inequigranular Qz-Fspmatrix, where Pl ($An_{40–52}$) andKfs ($Ab_{07–14}$) formthe framework microstructure (Fig. 4g,h).

Locally, an intense metamorphic overprint is documented in the melanosome portions and typified by symplectites of Crd-Sp-Pl-Qz ± Ilm developed at the expenses of early Grt-Ky-Rt assemblages (Fig. 4i). A post-kynematic growth of Bt-Sil±Ms±late Chl aggregates also occurs in secondary foliation replacing the early Grt-Ky-bearing texture.

6. Chemical zoning in garnet

Garnet in both melanosomes and melt segregates is essentially a zoned almandine-pyrope-grossular solid solution with a minor content of spessartine. The zoning profiles are characterized by marked Ca and Mg compositional zoning as illustrated in Fig. 5a. The Grt-1 grains are

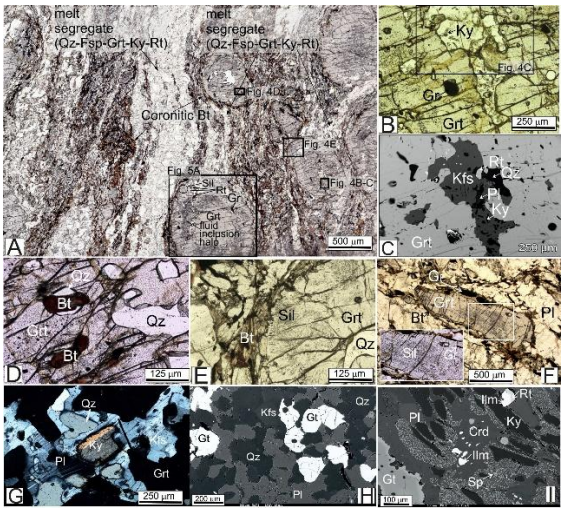

Fig. 4. Microtextures and mineral assemblages. (a) Scanned thin section of a melanosome-leucosome layering, showing the textural characteristics and arrangement of the Grt-1 types (sample K3). (b) Enlargement of the garnet core shown in Fig. 4a, showing the inclusion assemblages hosted at the garnet core. Plane polarised light. (c) Back-scattered electron (BSE) image showing of the area indicated in (b) showing the polymineralic and single-phase inclusion assemblage made of Rt, Qz, Kfs, Pl, Ky, Gr. (d) High-Ti Bt crystals hosted in poikiloblastic Grt-1 inner rim domain (area indicated in Fig. 4a). Bt inclusions occur together with rounded, single-phase, Qz inclusions. Plane polarised light. (e) Detail of a Grt-1 outer rim domain (area indicated in Fig. 4a), showing sillimanite inclusion. Plane polarised light. (f) Grt-2 in leucosome. The enlargement shows the sillimanite inclusion at the garnet core (sample Ma48). Plane polarised light. (g) The mineral assemblage in leucosomes, showing a well annealed Qz-Fsp-Qz matrix showing equilibrium textures with Ky and garnet (Grt-3; sample K3L). Crossed polarised light. (H) BSE image to illustrate the leucosomes microtexture (sample Ma09/28 L). Note the crystal framework made by plagioclase, with K-feldspar, quartz. Garnet (Grt-3) occurs as an interstitial phase with subhedral habit (sample Ma09/30 L). (h) BSE image showing evidence of the retrograde metamorphism, as documented by spinel–cordierite symplectic intergrowths that replaces early garnet-kyanite assemblages (sample K3M). Mineral abreviations follow Whitney and Evans (2010).

characterized by rather heterogeneous composition profiles, with a marked core-to-rim chemical zonation. When preserved, they show a broad core that is relatively homogeneous with respect to Fe and Mn ($Alm_{63–66}Pyr_{15–21}Grs_{15–17}Sps_{04–05}$), typically high in Ca and with the Mg content inversely correlated to the Ca content. In other cases, the Ca-rich core of Grt-1 is present only as relic (Fig. 5b) or completely lacking. The transition to the rim domains is characterized by a broad Ca-poor and Mg-rich domain ($Alm_{63–66}Pyr_{27–30}Grs_{05–07}Sps_{01–02}$), in conjunction with the transition from inclusion-free to inclusion–rich rim growth domains. The inclusion often contains a composite Qz-Fsp-Rt-Gr assemblage with Ky in addition. The occurrence of Sil is instead restricted to the outer rim zones of Grt-1 (Fig. 5a, b). The Grt-2 shows a nearly uniform core-to-rim composition with the core broadly corresponding to the Grt-1 outer rim compositions. Towards the rim, Ca increases at the expense of Mg and Fe. A variably developed (up to 50–70 µm large) outer rim showing a strong decrease ofMg and Ca, concomitant with a slight increase in the Mn component ($Alm_{58–64}Pyr_{25–27}Grs_{15–17}Sps_{06–07}$) (Fig. 5c). The Grt-3 shows a contrasting zoning pattern being characterized by a large homogeneous core rich in Ca and Mg ($Pyr_{26}Grs_{15}$; similar to the composition of the Grt-2 rims) that grades into a relatively narrow rim with lower contents of Ca and Mg and higher Mn (Fig. 5d).

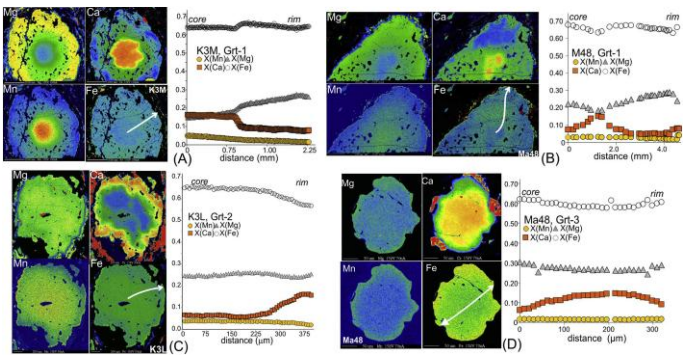

Fig. 5. Representative qualitative compositional maps and quantitative EMPA profiles showing variation in cations (Mn, Mg, Fe, Ca) distribution in garnet grains from the Beni Bousera granulite units. (a)-(b) Grt-1. (c) Grt-2. (c) Grt-3.

7. Whole-rock geochemistry

The chemical composition of four melanosome and five leucosome samples from the studied granulite migmatites (see Table 1 for sample location and constituent mineralogy) were analysed for major and

trace element geochemistry. Data are reported in Table 2 and graphically shown in Fig. 6 for the leucosome compositions.
The leucosomes have acidic composition (SiO_2=70.51–76.62wt%), associated with low MgO (0.09–0.35 wt%), FeO_{TOT} (0.96–2.06 wt%), TiO_2 (0.01–0.14 wt%) and CaO (1.14–2.01 wt%) contents. They are enriched in K_2O (5.29–5.57 wt%) with respect to Na_2O (1.7–2.78 wt%) and with an Al_2O_3 content of 12.26–15.50 wt%. In the TAS (total alkali vs. silica) diagram, the leucosomes fall in the granite field (Fig. 6a). Significantly, the leucosome compositions fall within those derived from experimental melts produced by biotite dehydration (Gao et al., 2016 and references therein) (Fig. 6b). Leucosome compositions are however K-depleted and show higher Ca/(Ca + Na) ratios than those of experimental and natural anatectic glasses (Fig. 6c,d; Taylor et al., 2014 and references therein). Melanosomes show SiO_2 ranging 41–63 wt% with high Al_2O_3 (16.7–28.8 wt%) and Fe_2O_{3TOT} (7.6–16.92 wt%) and low TiO_2 (1.0–1.4 wt%), associated with moderate MgO (2.1–4.2 wt%) and K_2O (2.1–3.1 wt%), variable CaO (0.8–4.1 wt%) and Na_2O (0.3–2.3 wt%). These compositions are strongly Si and K depleted and strongly enriched in Ca/(Ca+Na) ratios and Fe+Mg contents with respect to leucosomes (Fig. 6c,d).
The abundance of large-ion lithophile elements (LILEs, such as Ba, Rb, Sr) is positively correlated with SiO_2 and it is higher in leucosomes. Conversely, high-field strength elements (such as REE, Y, Nb and Zr) are negatively correlated with SiO_2 and their content is higher in melanosomes. When normalized to chondrite (after Sun and McDonough, 1989), all samples are generally enriched in light REE (LREE), with $(La/Sm)_N$ and $(La/Yb)_N$ ranging 3.09–7.40 and 1.73–5.68 for the leucosomes and 3.87–4.33 and 6.35–12.57 for themelanosome, respectively. The Eu anomaly ($Eu_N/[Sm_N \times Gd_N]_{1/2}$) is systematically positive for leucosomes (4.37–13.53),whereas in melanosomes varies from positive (2.64) to slightly negative (0.47), when moving from intermediate to low-silica compositions, respectively (Fig. 7).

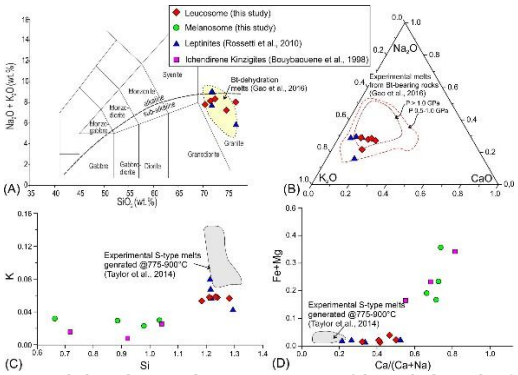

Fig. 6. Whole-rock major element composition of the studied samples. (a) Total alkali vs. silica (TAS) chemical classification diagram (LeMaitre et al. 2002) for the melt products interlayered within the Beni Boussera granulites. (b) The same samples plotted in the CaO–Na_2O–K_2O ternary diagram and compared to experimental melts produced through fluid absent biotite-dehydration melting. (c),(d) The major element compositions (100 wt% normalized) plotted as atomic K vs. Si and Ca/(Ca+Na) and vs. Fe+Mg (after Taylor et al., 2014).

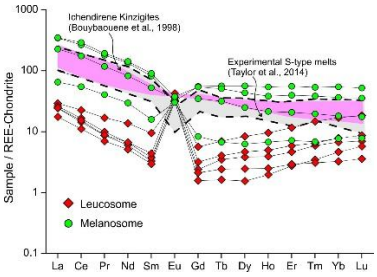

Fig. 7. Chondrite-normalized (after Sun and McDonough, 1989) REE patterns of the studied leucosome samples compared to the experimental S-type melts (after Taylor et al., 2014).

Table 2 - Whole rock chemical compositions

	Leucosome[*]						Melanosome[*]	Melanosome-leucosome Layering		
(wt%)	Ma09/28L	Ma09/30	K1	K2	K3L	Av(K1-K2-K3L)[#]	K3M	MA09/28M	MA09/32	B
SiO_2	76.62	74.72	71.98	70.51	71.51	71.33	41.01	58.19	52.28	63.08
Al_2O_3	12.26	14.42	14.84	15.41	15.50	15.25	28.82	16.7	23.81	18.36
$Fe_2O_{3(t)}$	0.96	1.29	1.26	2.06	1.58	1.63	16.92	8.2	12.41	7.66
MnO	0.024	0.027	0.06	0.09	0.04	0.06	0.429	0.072	0.294	0.13
MgO	0.09	0.33	0.16	0.35	0.24	0.25	4.18	3.52	3.02	2.11
CaO	1.14	1.56	1.88	2.01	1.76	1.88	1.47	4.13	0.85	2.1
Na_2O	2.62	1.7	2.78	2.57	2.67	2.67	0.57	2.29	0.35	0.92
K_2O	5.42	5.57	5.48	5.29	5.43	5.40	3.09	2.16	2.73	2.88
TiO_2	0.016	0.141	0.02	0.01	0.02	0.01	1.437	1.463	1.427	1.001
P_2O_5	0.1	0.14	0.12	0.18	0.13	0.14	0.07	0.03	0.1	0.19
LOI	0.24	0.68	0.12	0.09	0.23	0.15	2.54	2.89	2.1	2.18
Total	99.49	100.58	98.70	98.57	99.11	98.79	100.54	99.65	99.37	100.61
A/CNK	1.00	1.24	1.07	1.13	1.15	1.12	4.14	1.23	4.69	2.17
(ppm)										
Sc	1	1	3	6	3		54	17	32	18
Be	< 1	< 1	< 1	4	< 1		2	1	1	1
V	< 5	< 5	< 5	< 5	< 5		358	269	264	167
Cr	< 20	< 20	< 20	< 20	< 20		270	220	180	110
Co	< 1	< 1	< 1	1	< 1		39	32	33	19
Ni	< 20	< 20	< 20	< 20	< 20		90	60	70	50
Cu	< 10	< 10	< 10	< 10	< 10		30	100	40	40
Zn	< 30	< 30	< 30	< 30	< 30		190	160	180	110
Ga	10	10	11	17	14		34	23	42	23
Ge	2.2	1.5	2.5	2.7	1.6		4.1	0.5	3.1	1.7
As	< 5	< 5	< 5	< 5	< 5		< 5	< 5	5	< 5
Rb	148	10	134	124	158		120	97	118	113
Sr	239	215	268	335	261		119	195	89	167
Y	4.2	3.6	6.9	16.2	7.1		84.6	10	57.3	36.3
Zr	9	72	4	3	5		398	248	291	235
Nb	< 0.2	< 0.2	< 0.2	< 0.2	0.3		21.4	19.9	20.1	15.8
Mo	< 2	< 2	< 2	< 2	< 2		< 2	3	3	< 2
Ag	< 0.5	3.9	< 0.5	< 0.5	< 0.5		1.5	< 0.5	< 0.5	< 0.5
In	< 0.1	< 0.1	< 0.1	< 0.1	< 0.1		0.1	< 0.1	< 0.1	< 0.1
Sn	< 1	< 1	< 1	< 1	< 1		< 1	< 1	< 1	1
Sb	< 0.2	< 0.2	< 0.2	< 0.2	1.6		< 0.2	< 0.2	1.6	< 0.2
Cs	2.1	0.2	1.2	0.5	1.6		1.1	0.5	1.3	0.6
Ba	676	41	736	822	722		770	389	598	752
La	4.14	6.18	5.73	6.89	5.79		81.9	15.4	82.8	53.8
Ce	6.76	10.1	8.76	13.8	9.35		163	33.4	178	107
Pr	0.66	0.94	0.82	1.6	0.83		17.1	3.84	18.3	11.2
Nd	2.38	3.07	2.78	6.38	3.11		62.5	13.8	66.5	38.5
Sm	0.45	0.57	0.5	1.44	0.67		12.5	2.42	13.8	8.03
Eu	1.8	1.89	2.11	1.84	2.46		1.84	1.75	2.18	2.03
Gd	0.43	0.32	0.49	1.15	0.65		11.3	1.7	11.1	7.13
Tb	0.09	0.06	0.13	0.26	0.15		2.11	0.25	1.89	1.18
Dy	0.62	0.39	0.97	2.12	1.18		14.3	1.58	11	6.31
Ho	0.14	0.11	0.22	0.54	0.28		3.06	0.38	2.16	1.21
Er	0.48	0.45	0.76	1.91	0.97		9.19	1.18	6.54	3.42
Tm	0.078	0.088	0.15	0.374	0.165		1.36	0.173	0.978	0.498
Yb	0.55	0.78	1.14	2.86	1.32		9.25	1.3	6.18	3.07
Lu	0.09	0.145	0.176	0.466	0.219		1.32	0.197	0.902	0.444
Hf	0.2	23.5	< 0.1	< 0.1	0.2		10.2	6.1	7.8	5.7
Ta	0.08	< 0.01	0.02	0.02	0.03		1.42	1.23	1.17	1.08
W	1.1	< 0.5	< 0.5	< 0.5	0.5		< 0.5	< 0.5	< 0.5	0.9
Tl	0.61	0.13	0.67	0.61	0.85		0.5	0.28	0.88	0.71
Pb	39	10	64	39	89		18	< 5	17	17
Bi	< 0.1	< 0.1	< 0.1	< 0.1	< 0.1		< 0.1	< 0.1	0.1	8.9
Th	0.11	0.34	0.41	0.11	0.45		22.6	2.52	31.2	17
U	0.15	2.61	0.25	0.15	0.36		1.86	0.99	2.03	1.38
(La/Sm)N	5.94	7.00	7.40	3.09	5.58		4.23	4.11	3.87	4.33
(La/Yb)N	5.40	5.68	3.61	1.73	3.15		6.35	8.50	9.61	12.57
Eu/Eu*	12.51	13.53	13.03	4.37	11.40		0.47	2.64	0.54	0.82
[a] T_{Zr}(°C)	585	738	541	529	557					

[*] Grey shaded whole rock compositions are used for the pseudosection modelling

[#] Average whole rock compositions used for the pseudosection modelling

[a] T_{Zr} (°C) = Zircon saturation thermometry (Watson and Harrison, 1983)

8. U-Pb zircon geochronology

The zircon U-Pb geochronological study was carried out on zircon separates as obtained from a melanosome-leucosome layering (sample K3L, representative of the in situ melt segregates) and two leucosomes (sampleMa09/28 L and Ma09/30 L as representative ofmeltmobilisates). Sample Ma09/28 L is from an in situ melt segregation, while Ma09/30 is froma boudinated granite (Fig. 3). Sample K3L is located within the alteration zone associatedwith dyke emplacement at the base of the granulite exposure (Fig. 3).

Zircon grains were investigated through cathodoluminescence (CL) and back scattered electron (BSE) imaging techniques and subsequently analysed in situ through a LA-ICP-MS system at the Frankfurt Isotope and Element Research Center (FIERCE) of the Goethe University of Frankfurt (see Supplementary Material 1). Analytical results are shown in Table 3a–c. Age calculations and graphical display were obtained through the ISOPLOT software (Ludwig, 2003).

8.1. Sample K3L

Zircons are generally euhedral to subhedral. Based on the BSE and CL imaging, two textural types are defined. The first and more abundant type consists of moderately luminescent, single-phase zircons with oscillatory zoning and planar growth banding (Fig. 8a). The second type comprises grains with distinct core and rim structures. The cores (inner and outer) show oscillatory and sector zoned growth zoning and are embayed by thin (10–30 μm wide), low-luminescent rims that commonly truncate the inner zoning (Fig. 8a). Minor metamict textures are also observed in some grains, documented by opaque, fractured domains. The Th/U values vary largely, with values significantly higher in the growth zoning domains (up to 0.70) with respect to the low-luminescent rims (b0.01) (Table 3; Fig. 9).

The range of analytical zircon ages is very large, with apparent $^{206}Pb/^{238}U$ ages spanning from the Late Archean (ca. 2.5 Ga) in the cores to Cenozoic (ca. 22 Ma) in the structureless rim domains. However, a significant age cluster from the oscillatory growth domains is observed at c. 300 Ma (Table 3; Fig. 8a). Taking into account the age population younger than 300 Ma, data array defines a Discordia with an upper intercept at 297 (+16/ − 17) Ma and a lower intercept of

early Miocene age, at 20.0 (+4.4/ − 4.8) Ma. Eight analyses from the low-luminescent structureless rims form a nearly concordant age cluster at the lower end of the Discordia, yielding a weighted mean $^{206}Pb/^{238}U$ age of 22.1 ± 0.4 (Fig. 8a).

8.2. Sample Ma09/30L

Zircons are generally euhedral to subhedral. Most zircon grains show short to long prismatic habits (usually N250 μm), with length/width ratios up to 5:1. They appear as nearly homogeneous in BSE images. In CL images, zircons are weakly luminescent and show oscillatory to sector (soccer ball) growth zoning (Fig. 8b), typical of igneous zircons (Corfu et al., 2003; Harley et al., 2007). No inherited cores are present. The U content of these growth domains is moderate to high (330–1340 ppm) and the Th/U is generally low (0.02–0.01) (Table 3; Fig. 9). The probability distribution plot of the cumulative eighty-six spots provides a mean cluster of $^{206}Pb/^{238}U$ ages at 294 ± 1 Ma (2σ; 79% of the data). Thirty-three spots define a near concordant group, intercepting the Concordia curve at 301 ± 2 Ma Ma (2σ, MSWD = 4.4) (Fig. 8b).

8.3. Sample Ma09/28 L

Zircons are typically long prismatic in shape and euhedral. A minor aliquot shows a pyramidal shape. They are homogeneous in BSE and the CL images reveal dominant oscillatory to sector growth zoning (Fig. 8c), typical of igneous zircons. Also in this case, no inherited cores are present. The Th/U values range 0.01–0.22 (Table 3; Fig. 9). The probability distribution plot of the cumulative thirty-two spots provides a mean cluster of $^{206}Pb/^{238}U$ ages at 290 ± 1 Ma (2σ; 81% of the data). Twenty-nine spots define a Concordia age at 291 ± 1 Ma (2σ, MSWD= 1.3) (Fig. 8c).

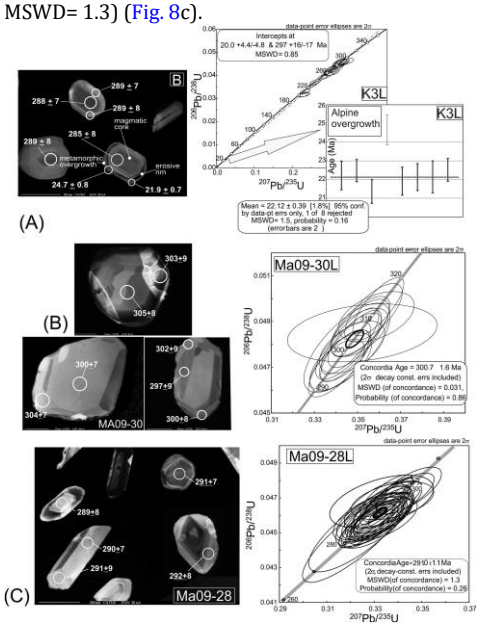

Fig. 8. (a)–(c) Cathodoluminescence images with location of the LA-ICPM laser spots (white circles) indicated (all ages are 206Pb/238U ages in Ma, with errors quoted at 2σ level) and conventional Concordia diagrams of the analysed zircon grains from the studied samples (see Table 3). The inset in (a) shows the weighted average of 206Pb/238U ages for the data population at the lower end of the Discordia.

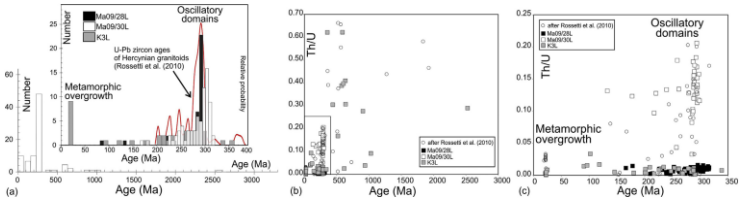

Fig. 9. (a) Probability age distribution plot as obtained fromthe cumulative $^{206}Pb/^{238}U$ zircon age data. (b),(c) $^{206}Pb/^{238}U$ ages vs. U/Th diagramvalues for the analysed zircon ages. Data are compared with those available from the Hercynian leptinites intruded into the Lower Sebtides units (after Rossetti et al., 2010).

Table 3 - Results of U-Th-Pb LA-ICP-MS analyses and calculated ages for zircon separates from the migmatitic granulites of the Beni Bousera unit

Sample K3L - melanosome/leucosome layering

															Age (Ma)					
grain	L-No.	Texture/Position	$^{207}Pb^a$ (cps)	U^b (ppm)	Pb^b (ppm)	Th^b U	$^{206}Pb/^{204}Pb$	$^{206}Pb/^{238}U$	±2σ (%)	$^{207}Pb/^{235}U$	±2σ (%)	$^{207}Pb/^{206}Pb$	±2σ (%)	Rho ^{d}	$^{206}Pb/^{238}U$	±2σ	$^{207}Pb/^{206}Pb$	±2σ	$^{207}Pb/^{206}Pb$	±2σ
z5	a1	oscillatory/core	5082	562	18	0.033	24824	0.0361	3.2	0.256	4.1	0.0514	2.6	0.77	229	7	231	9	257	60
z6a	a2	oscillatory/core	5328	491	18	0.037	5762	0.0401	3.0	0.291	4.4	0.0526	3.2	0.68	254	7	259	10	314	73
z6b	a3	oscillatory/rim	2965	391	15	0.034	19408	0.0414	2.3	0.293	3.6	0.0513	2.7	0.66	261	6	261	8	254	62
Z7a	a4	oscillatory/core	3239	371	13	0.021	4254	0.0391	2.8	0.279	4.0	0.0517	2.9	0.69	247	7	250	9	273	66
Z7b	a5	oscillatory/rim	5131	1000	41	0.032	24555	0.0446	2.8	0.322	3.9	0.0523	2.7	0.72	281	8	283	10	300	61
Z8a	a6	overgrowth/rim	1102	806	2.6	0.004	5556	0.00345	3.4	0.022	8.2	0.0467	7.4	0.42	22.2	0.8	22.3	1.8		
Z8a1	a7	overgrowth/rim	1184	716	2.3	0.002	2804	0.00349	2.6	0.023	17.5	0.0476	17	0.15	22.5	0.6	23.0	4.0		
Z8a2	a8	oscillatory/core	1983	263	7.7	0.031	9370	0.0318	2.6	0.231	5.7	0.0527	5.0	0.46	202	5	211	11	316	115
Z8b	a9	oscillatory/core	3373	357	13	0.030	6851	0.0411	2.5	0.301	4.3	0.0531	3.4	0.60	260	6	267	10	333	78
Z8b1	a10	overgrowth/rim	1244	688	2.1	0.010	6282	0.00332	3.0	0.021	6.9	0.0466	6.2	0.43	21.4	0.6	21.4	1.5		
Z9a	a11	oscillatory/core	2689	591	20	0.041	13144	0.0370	2.8	0.260	4.4	0.0509	3.4	0.63	234	6	235	9	237	80
Z9a1	a12	overgrowth/rim	3136	312	12	0.022	14823	0.0432	3.6	0.316	5.0	0.0531	3.5	0.72	272	10	279	12	332	79
Z4a	a13	oscillatory/core	2682	362	11	0.041	8882	0.0330	2.6	0.233	4.6	0.0513	3.8	0.56	209	5	213	9	253	87
Z4a1	a14	oscillatory/rim	6875	1280	49	0.013	33464	0.0422	3.5	0.301	4.5	0.0517	2.8	0.78	267	9	267	11	270	64
Z4a2	a15	oscillatory/rim	4167	969	38	0.010	20189	0.0426	3.3	0.302	4.6	0.0514	3.2	0.72	269	9	268	11	257	73
Z4b	a16	oscillatory/rim	1067	701	30	0.005	5026	0.0461	2.6	0.337	5.9	0.0531	5.3	0.44	291	7	295	15	332	121
Z4b1	a17	oscillatory/core	3490	360	14	0.031	16450	0.0414	2.7	0.303	5.4	0.0531	4.7	0.51	261	7	269	13	335	106
Z4b2	a18	oscillatory/rim	1935	202	8.4	0.018	4459	0.0450	2.7	0.326	4.9	0.0524	4.1	0.55	284	8	286	12	305	94
Z2a	a19	overgrowth/rim	1170	411	1.5	0.027	3325	0.00383	3.3	0.0267	6.7	0.0505	5.9	0.49	24.7	0.8	26.7	1.8		
Z2a1	a20	overgrowth/rim	1136	357	1.2	0.008	5707	0.00340	3.4	0.0216	6.4	0.0460	5.4	0.53	21.9	0.7	21.7	1.4		
Z2a2	a21	oscillatory/core	6756	454	18	0.034	22440	0.0441	2.5	0.324	3.2	0.0532	2.0	0.79	278	7	285	8	337	44
Z2b	a22	oscillatory/core	5387	508	21	0.036	26145	0.0458	2.5	0.327	4.2	0.0519	3.4	0.59	289	7	288	11	279	78
Z2b1	a23	oscillatory/rim	2355	234	10	0.022	11287	0.0458	2.7	0.330	4.8	0.0523	4.0	0.56	289	8	290	12	299	91
Z2b2	a24	oscillatory/rim	1909	192	8.1	0.027	6790	0.0457	2.5	0.333	4.4	0.0528	3.5	0.58	288	7	292	11	321	80
Z10a	a25	overgrowth/rim	1115	332	1.1	0.014	3105	0.00344	3.3	0.0218	8.1	0.0459	7.4	0.40	22.1	0.7	21.9	1.8		
Z10a1	a26	oscillatory/core	4115	487	20	0.024	19960	0.0457	3.1	0.326	4.5	0.0517	3.3	0.69	288	9	286	11	272	75
Z10a2	a27	overgrowth/rim	1177	392	1.3	0.009	5702	0.00344	3.9	0.0229	7.2	0.0483	6.1	0.54	22.1	0.9	23.0	1.6	113	143
Z14a	a28	overgrowth/rim	1215	719	2.3	0.007	6209	0.00350	2.7	0.0216	9.2	0.0448	8.8	0.29	22.5	0.6	21.7	2.0		
Z14a1	a29	oscillatory/core	3765	465	13	0.013	18052	0.0316	2.4	0.230	4.4	0.0527	3.6	0.55	201	5	210	8	318	83
Z2a	a30	overgrowth/rim	2312	382	10	0.012	6245	0.0284	3.6	0.207	4.7	0.0530	3.0	0.77	180	6	191	8	328	68
Z2a1	a31	overgrowth/rim	1689	263	3.6	0.046	3282	0.0142	7.4	0.102	8.2	0.0520	3.5	0.90	91	7	98	8	286	80
Z2a2	a32	oscillatory/core	1840	74	7.1	0.44	7441	0.0936	2.4	0.783	4.1	0.0607	3.3	0.58	577	13	587	18	627	71
Z2b	a33	outer rim	2683	90	6.0	0.71	7667	0.0567	3.2	0.426	4.7	0.0546	3.4	0.68	355	11	361	14	395	76
Z2b1	a34	inner rim	3533	275	14	0.025	16303	0.0539	2.6	0.397	3.7	0.0534	2.6	0.70	339	9	339	11	344	60
Z2b2	a35	oscillatory/core	2762	229	4.8	0.016	3569	0.0229	4.4	0.166	5.2	0.0526	2.8	0.84	146	6	156	8	311	64
Z3a	a36	oscillatory/core	5316	237	25	0.71	21942	0.0957	2.0	0.809	3.2	0.0613	2.5	0.63	589	12	602	15	649	54
Z3a1	a37	overgrowth/rim	1302	45	0.7	0.11	3933	0.0160	4.8	0.116	6.0	0.0528	3.7	0.80	102	5	112	6	321	83
Z3b	a38	overgrowth/rim	3941	593	19	0.008	12221	0.0342	3.8	0.242	4.7	0.0512	2.8	0.81	217	8	220	9	251	63
Z3b1	a39	oscillatory/core	4628	206	15	0.35	21575	0.0706	3.6	0.592	4.3	0.0608	2.2	0.85	440	15	472	16	632	48
Z4a	a40	oscillatory/core	9684	380	41	0.47	40113	0.103	2.9	0.868	4.3	0.0610	3.2	0.68	634	18	635	20	638	68
Z4a1	a41	oscillatory/core	3964	156	16	0.35	16776	0.104	3.1	0.860	4.1	0.0600	2.7	0.75	637	19	630	19	604	58
Z4a2	a42	overgrowth/rim	764	145	5.1	0.028	2268	0.0357	4.9	0.278	6.6	0.0566	4.4	0.74	226	11	249	15	475	98
Z8a	a43	luminescent inner rim	3413	169	26	0.044	8419	0.157	5.5	2.21	6.4	0.102	3.2	0.87	938	48	1185	45	1669	58
Z8a1	a44	overgrowth/rim	2217	185	17	0.029	9041	0.100	5.4	0.856	6.4	0.0619	3.4	0.85	616	32	628	30	672	72
Z8a2	a45	oscillatory/core	10047	244	42	0.11	22595	0.173	5.3	2.51	6.0	0.105	2.7	0.89	1029	51	1274	44	1714	50
Z8b	a46	oscillatory/core	6047	94	15	0.32	15014	0.151	3.9	2.10	4.7	0.101	2.7	0.82	906	33	1150	33	1647	50
Z7a	a47	oscillatory/core	12376	30	17	0.33	13268	0.480	2.6	15.5	3.4	0.234	2.3	0.74	2526	54	2846	33	3080	37
Z7a1	a48	overgrowth/rim	466	204	2.9	0.049	2138	0.0151	7.2	0.114	11.4	0.0550	8.9	0.63	96	7	110	12	412	198
Z6a	a49	oscillatory/core	3584	248	26	0.45	13822	0.0982	7.8	0.846	8.8	0.0624	4.2	0.88	604	45	622	42	689	89
Z6a1	a50	inner rim	1834	306	5.3	0.054	3364	0.0185	6.4	0.137	7.3	0.0536	3.7	0.87	118	7	130	9	355	83
Z6a2	a51	overgrowth/rim	12410	457	1.5	0.015	4573	0.00350	5.4	0.0222	6.0	0.0460	2.6	0.90	22.5	1.2	22.3	1.3		
Z6b	a52	oscillatory/core	3277	142	12	0.19	13405	0.0837	3.9	0.710	5.5	0.0615	3.9	0.70	518	19	545	23	656	84

Sample MA09/30L - leucosome

															Age (Ma)					
grain	L-No.	Texture/Position	$^{207}Pb^a$ (cps)	U^b (ppm)	Pb^b (ppm)	Th^b U	$^{206}Pbc^c$ (%)	$^{206}Pb^d/^{238}U$	±2σ (%)	$^{207}Pb^d/^{235}U$	±2σ (%)	$^{207}Pb^d/^{206}Pb$	±2σ (%)	rho ^{e}	$^{206}Pb/^{238}U$	±2σ (Ma)	$^{207}Pb/^{238}U$	±2σ (Ma)	$^{207}Pb/^{206}Pb$	±2σ (Ma)
z1	A04	oscillatory/core	4336	329	8	0.01	0.0	0.02611	2.8	0.1902	4.8	0.05283	3.9	0.58	166	5	177	8	322	89
z1	A05	oscillatory/rim	8786	464	17	0.01	b.d.	0.03996	4.4	0.2945	4.8	0.05164	1.8	0.92	253	11	254	11	269	42
z2	A06	oscillatory/core	7977	389	18	0.01	0.0	0.05016	2.3	0.3564	3.0	0.05154	1.9	0.77	315	7	310	8	265	44
z2	A07	oscillatory/core	6747	360	16	0.01	b.d.	0.04965	2.1	0.3597	2.7	0.05254	1.7	0.78	312	6	312	7	309	38
z3	A08	oscillatory/core	8719	436	19	0.01	0.0	0.04814	2.5	0.3466	3.2	0.05222	2.0	0.78	303	7	302	8	295	45
z3	A09	oscillatory/core	8722	429	19	0.01	0.0	0.04717	2.6	0.3414	3.4	0.05250	2.2	0.75	297	7	298	9	307	51
z3	A10	oscillatory/rim	20811	484	23	0.01	6.5	0.04547	1.9	0.3369	6.3	0.05374	6.0	0.30	287	5	295	16	360	136
z4	A11	oscillatory/rim	21292	1121	35	0.00	0.3	0.03371	4.3	0.2470	5.0	0.05313	2.5	0.86	214	9	224	10	334	57
z4	A12	oscillatory/core	8931	429	20	0.01	0.0	0.04991	2.4	0.3692	3.3	0.05365	2.4	0.70	314	7	319	9	357	54
z6	A13	oscillatory/core	9474	640	21	0.01	0.0	0.03654	1.8	0.2642	3.5	0.05245	3.0	0.51	231	4	238	8	305	69
z6	A14	oscillatory/rim	17782	1022	36	0.00	0.0	0.03897	4.1	0.2761	4.6	0.05138	2.2	0.88	246	10	248	10	258	51
z6	A15	oscillatory/core	8941	581	21	0.01	0.0	0.03973	2.3	0.2845	3.5	0.05194	2.6	0.67	251	6	254	8	283	60
z5	A16	oscillatory/core	7185	363	14	0.01	0.0	0.04328	3.4	0.3100	4.2	0.05196	2.5	0.80	273	9	274	10	283	57
z5	A17	oscillatory/core	8523	425	18	0.01	0.0	0.04680	2.4	0.3398	3.5	0.05266	2.5	0.68	295	7	297	9	314	58
z5	A18	oscillatory/rim	11215	608	24	0.01	0.1	0.04302	2.0	0.3105	2.4	0.05234	1.3	0.84	272	5	275	6	300	31
z5	A19	oscillatory/rim	9693	499	22	0.01	0.0	0.04728	1.9	0.3461	3.3	0.05310	2.7	0.58	298	6	302	9	333	61
z5	A20	oscillatory/rim	8386	430	19	0.01	0.2	0.04773	2.2	0.3434	3.0	0.05218	2.1	0.71	301	6	300	8	293	49
z7	A21	oscillatory/core	21081	1266	44	0.00	0.0	0.03779	3.0	0.2741	3.5	0.05262	1.9	0.84	239	7	246	8	312	44
z7	A22	oscillatory/core	21159	1306	46	0.00	0.0	0.03883	3.5	0.2831	3.9	0.05287	1.9	0.88	246	8	253	9	323	42
z7	A23	oscillatory/core	20855	1280	39	0.00	0.5	0.03309	3.3	0.2387	4.1	0.05232	2.4	0.81	210	7	217	8	299	54
z8	A26	oscillatory/core	8764	465	20	0.01	0.0	0.04751	1.9	0.3443	2.8	0.05256	2.1	0.67	299	6	300	7	310	48
z8	A27	oscillatory/core	56456	597	38	0.01	26	0.04367	3.7	0.3181	24.9	0.05292	24.6	0.15	276	10	280	63	321	559
z8	A28	oscillatory/rim	9595	505	22	0.01	0.1	0.04797	1.9	0.3496	2.7	0.05286	1.9	0.71	302	6	304	7	323	44
z8	A29	oscillatory/core	10079	517	21	0.01	0.8	0.04497	2.0	0.3229	3.6	0.05207	3.0	0.56	284	6	284	9	288	69
z23a	A30	oscillatory/rim	9764	479	19	0.01	2.5	0.04137	1.6	0.3020	3.8	0.05295	3.5	0.41	261	4	268	9	327	79
z23a	A31	oscillatory/core	13782	699	28	0.01	0.7	0.04380	2.0	0.3211	2.9	0.05317	2.1	0.70	276	5	283	7	336	47
z23a	A32	oscillatory/core	11920	679	26	0.01	0.0	0.04161	2.6	0.2980	3.1	0.05194	1.7	0.84	263	7	265	7	283	39
z23a	A33	oscillatory/core	11366	701	25	0.01	0.0	0.03843	1.7	0.2784	2.2	0.05255	1.4	0.78	243	4	249	5	309	32
z23b	A34	oscillatory/rim	13888	714	29	0.00	0.0	0.04427	2.6	0.3185	2.9	0.05218	1.3	0.90	279	7	281	7	293	29
z23b	A36	oscillatory/core	12087	594	26	0.01	0.0	0.04691	2.1	0.3418	3.2	0.05285	2.4	0.66	296	6	299	8	322	54
z23b	A37	oscillatory/rim	11458	575	25	0.01	0.0	0.04657	2.6	0.3421	3.3	0.05327	2.0	0.78	293	7	299	8	340	46
z23b	A38	oscillatory/core	13844	557	25	0.01	1.9	0.04787	2.0	0.3475	3.6	0.05265	3.0	0.55	301	6	303	9	314	68
z23b	A39	oscillatory/core	14852	569	25	0.01	1.8	0.04611	2.3	0.3399	3.8	0.05346	3.1	0.59	291	6	297	10	348	70
z11	A40	oscillatory/core	10759	539	23	0.01	0.0	0.04687	2.6	0.3419	3.6	0.05292	2.4	0.73	295	7	299	9	325	55
z11	A41	oscillatory/core	8271	430	18	0.02	0.0	0.04693	2.2	0.3413	3.0	0.05276	2.0	0.74	296	6	298	8	318	46
z11	A42	oscillatory/rim	20114	1193	47	0.00	0.3	0.04319	1.5	0.3101	2.4	0.05207	1.9	0.63	273	4	274	6	299	43
z11	A43	oscillatory/core	13580	771	31	0.00	0.0	0.04474	2.7	0.3264	3.2	0.05291	1.8	0.82	282	7	287	8	325	41
z22a	A44	oscillatory/rim	15885	578	26	0.01	3.2	0.04591	1.7	0.3359	4.3	0.05306	3.9	0.39	289	5	294	11	331	89
z22a	A45	oscillatory/core	10995	569	25	0.01	0.0	0.04818	2.3	0.3522	3.2	0.05302	2.2	0.73	303	7	306	8	330	49
z22a	A48	oscillatory/core	10592	549	24	0.01	0.2	0.04708	2.0	0.3406	3.1	0.05247	2.3	0.65	297	6	298	8	306	53
z22a	A49	oscillatory/rim	20907	538	26	0.01	5.4	0.04567	2.0	0.3301	5.8	0.05241	5.4	0.35	288	6	290	15	303	123
z22b	A50	oscillatory/core	11680	619	27	0.01	0.0	0.04818	2.0	0.3488	2.9	0.05251	2.1	0.69	303	6	304	8	308	48
z22b	A51	oscillatory/core	11449	618	26	0.01	0.0	0.04535	2.0	0.3305	2.5	0.05285	1.5	0.81	286	6	290	6	323	34
z22b	A52	oscillatory/rim	10883	595	26	0.01	0.0	0.04720	1.9	0.3373	3.0	0.05183	2.3	0.62	297	5	295	8	278	54
z13	A53	oscillatory/rim	10313	522	24	0.01	0.0	0.04939	2.1	0.3575	3.1	0.05250	2.2	0.69	311	6	310	8	307	50
z13	A54	oscillatory/core	7913	403	18	0.01	0.0	0.04764	1.9	0.3463	3.3	0.05271	2.7	0.57	300	5	302	9	316	61
z13	A55	oscillatory/core	30124	407	25	0.01	14.1	0.04896	2.4	0.3574	8.1	0.05295	7.7	0.30	308	7	310	22	327	176
z13	A56	oscillatory/rim	194123	546	77	0.01	47.1	0.04488	5.8	0.3341	17.8	0.05400	16.8	0.33	283	16	293	46	371	379
z13	A57	oscillatory/core	22272	509	26	0.01	6.2	0.04894	1.9	0.3665	5.1	0.05432	4.7	0.37	308	6	317	14	384	106
z14	A58	oscillatory/rim	20161	999	35	0.01	0.5	0.03773	2.7	0.2770	3.4	0.05324	2.1	0.78	239	6	248	8	339	48
z14	A59	oscillatory/core	5696	395	13	0.01	0.0	0.03572	2.6	0.2614	3.5	0.05309	2.4	0.74	226	6	236	7	332	54
z14	A60	oscillatory/core	8995	468	21	0.01	0.0	0.04895	2.2	0.3501	3.1	0.05188	2.2	0.71	308	7	305	8	280	50
z14	A61	oscillatory/core	10702	550	25	0.01	0.0	0.04874	2.2	0.3565	3.4	0.05304	2.5	0.65	307	7	310	9	331	58
z10	A62	oscillatory/core	9905	511	22	0.01	0.1	0.04793	2.7	0.3471	3.3	0.05251	2.0	0.80	302	8	303	9	308	45
z10	A63	oscillatory/core	8896	433	20	0.01	0.2	0.05026	2.1	0.3593	3.3	0.05186	2.5	0.64	316	7	312	9	279	58
z10	A64	oscillatory/rim	9622	371	17	0.01	1.7	0.04921	1.8	0.3588	4.0	0.05288	3.6	0.46	310	6	311	11	324	81
z10	A65	oscillatory/rim	24282	495	26	0.02	9.6	0.04850	2.1	0.3523	8.1	0.05268	7.8	0.26	305	6	306	22	315	177
z10	A66	oscillatory/core	6365	334	15	0.01	0.0	0.04852	1.8	0.3509	3.1	0.05245	2.6	0.57	305	5	305	8	305	58
z10	A67	oscillatory/rim	14067	507	23	0.01	2.9	0.04596	2.0	0.3384	4.3	0.05340	3.7	0.47	290	6	296	11	346	85
z9a	A70	structureless rim	5444	493	13	0.01	0.1	0.02803	2.2	0.1997	3.4	0.05168	2.6	0.64	178	4	185	6	271	60
z9a	A71	oscillatory/core	8573	448	19	0.01	0.0	0.04724	2.2	0.3423	3.4	0.05256	2.6	0.64	298	6	299	9	310	60
z9a	A72	oscillatory/core	10341	522	22	0.01	0.0	0.04671	3.4	0.3418	4.3	0.05307	2.7	0.79	294	10	299	11	332	60
z9b	A73	oscillatory/core	7582	424	15	0.01	0.1	0.03984	2.5	0.2876	3.9	0.05236	3.0	0.64	252	6	257	9	301	68
z9b	A74	oscillatory/core	12152	717	26	0.01	0.0	0.03941	3.1	0.2855	3.8	0.05254	2.3	0.81	249	8	255	9	309	51
z9b	A75	oscillatory/rim	8786	472	18	0.01	0.0	0.04179	2.5	0.3017	3.5	0.05236	2.4	0.71	264	6	268	8	301	55
z9c	A76	oscillatory/core	9132	458	20	0.01	0.1	0.04871	2.1	0.3513	3.1	0.05230	2.3	0.68	307	6	306	8	299	52
z9c	A77	oscillatory/core	9026	445	20	0.01	0.0	0.04847	2.4	0.3530	3.2	0.05282	2.1	0.74	305	7	307	8	321	48
z9c	A79	oscillatory/core	8742	449	20	0.01	0.1	0.04879	2.2	0.3514	3.2	0.05224	2.4	0.68	307	7	306	9	296	54
z19	A80	oscillatory/core	9948	441	20	0.01	1.4	0.04785	3.3	0.3452	4.7	0.05232	3.4	0.70	301	10	301	12	299	77
z19	A81	oscillatory/core	24888	467	26	0.01	9.5	0.04970	2.4	0.3545	7.6	0.05174	7.2	0.31	313	7	308	20	274	166
z19	A82	oscillatory/rim	48734	453	32	0.01	20.3	0.04943	3.0	0.3494	16.4	0.05127	16.1	0.18	311	9	304	44	253	371
z18a	A83	oscillatory/core	9189	471	21	0.01	0.0	0.04838	2.4	0.3546	3.3	0.05316	2.2	0.75	305	7	308	9	336	49
z18a	A84	oscillatory/rim	9060	468	21	0.01	0.0	0.04806	2.4	0.3497	3.3	0.05277	2.3	0.71	303	7	304	9	319	53
z18b	A85	oscillatory/core	8960	402	18	0.01	1.0	0.04864	2.6	0.3589	3.6	0.05352	2.5	0.72	306	8	311	10	351	56
z18b	A86	oscillatory/rim	6987	400	15	0.01	0.0	0.04205	2.4	0.3052	3.4	0.05264	2.5	0.68	266	6	270	8	313	57
Plesovice[f]			9782	419	21	0.13	0.08	0.053988	1.49869	0.3970	2.6	0.053331	1.202127	0.626486	338.9607	5	339.4659	7	342.8504	27
91500[f]			7049.96	63	12	0.39	0.32	0.1796	1.5	1.8526	1.6	0.074824	1.617275	0.622326	1064.667	14	1064.365	11	1063.747	33

Sample Ma09/28L - leucosome

															Age (Ma)					
grain	L-No.	Texture/Position	$^{207}Pb^a$ (cps)	U^b (ppm)	Pb^b (ppm)	Th^b U	$^{206}Pbc^c$ (%)	$^{206}Pb^d/^{238}U$	±2σ (%)	$^{207}Pb^d/^{235}U$	±2σ (%)	$^{207}Pb^d/^{206}Pb$	±2σ (%)	rho ^{e}	$^{206}Pb/^{238}U$	±2σ (Ma)	$^{207}Pb/^{238}U$	±2σ (Ma)	$^{207}Pb/^{206}Pb$	±2σ (Ma)
z14	a23	core	146843	987	42	0.13	0.02	0.0443	2.5	0.3186	2.9	0.05216	1.5	0.85	279	7	281	7	293	35
z14	a24	oscillatory/rim	55743	396	18	0.12	1.21	0.04602	2.2	0.3338	3.1	0.05261	2.2	0.71	290	6	292	8	312	50
z13	a25	rim	43784	360	14	0.04	0.96	0.0407	2.6	0.2901	3.3	0.0517

9. Zircon and garnet REE chemistry

Zircon and garnet crystals from the same samples used for U-Pb zircon geochronology (Table 1), were analysed both on mineral separates and in thin sections for REE and trace element determination by LA-ICPMS at the Institut fur Mineralogie, Universitat Stuttgart (see Supplementary Material#1). The analysed spots in zircons correspond to the oscillatory or sector growth zoning domains analysed for the U\\Pb geochronology. The different garnet growth domains in igneous Grt-2 (core and rims) and Grt-3 (cores) grains were analysed. The results are presented in Fig. 10 and Table 4.

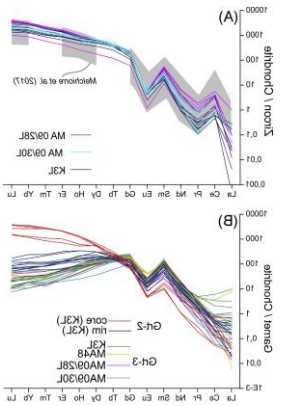

Fig. 10. Chondrite-normalized (Sun and McDonough, 1989) REE pattern of the (a) analysed zircons and (b) garnets.

9.1. Zircon

The analysed spots areas correspond to the same sector-zoned or oscillatory growth domains investigated for the U-Pb geochronology.

Irrespective of the sample, all the analysed zircon domains (22 spots) are characterized by low LREE (ΣLREE of 0.74–6.9 ppm, with a mean value of 2.4 ppm) and high HREE (ΣHREE ranging 335–1264 ppm, average value: 894 ppm) contents, respectively. They show chondrite normalized (Sun and McDonough, 1989) depleted LREE (average La_N = 0.40 and La_N/Sm_N b 0.15) and enriched HREE (average Yb_N: 21745 and Dy_N/Yb_N values of 0.19–0.38) patterns. All analysed zircons show a systematic negative Eu anomaly (0.05–0.11). The observed REE patterns are fully compatible with those presented in Melchiorre et al. (2017) (Fig. 10a).

The Ti contents of the zircons were also analysed in order to constrain the temperature at which the zircons grew using the Ti-in-zircon thermometer (Watson and Harrison, 2005; Watson et al., 2006). The measured Ti values range between 3.4 and 13.8 ppm, corresponding to a temperature estimate of 654–770 °C (Table 4), provided that rutile was present at the time of zircon crystallisation.

9.2. Garnet

The Grt-2 cores (6 spots) are characterized by low LREE (ΣLREE ranging 0.54–8.2 ppm, average value of 2.8 ppm) and elevated HREE (ΣHREE ranging 552–1366 ppm) contents. They are characterized by extremely depleted chondrite-normalized LREE (La_N/Sm_N b 0.002) and enriched HREE patterns (Yb_N/Gd_N: 8–38) (Fig. 10b). The Grt-2 rims (9 spots) show comparable low LREE (ΣLREE: 3.0–9.8 ppm) but lower HREE (ΣHREE of 81–219 ppm) contents. They show similar LREE (La_N/Sm_N b 0.007) depletion, together with a less evident HREE enrichment (Yb_N/Gd_N: 0.42–2.9). Both the Grt-2 cores and rims show a systematic negative Eu/Eu* anomaly (0.17 and 0.19, average value of cores and rims, respectively) (Fig. 10b).

The Grt-3 garnets (cores, 22 spots) are characterized by moderate LREE (ΣLREE of 1.8–12 ppm) and elevated HREE (ΣHREE of 53–181 ppm) contents, with depleted chondrite-normalized LREE (La_N/Sm_N b 0.1) and HREE (Yb_N/Gd_N b 0.9) patterns and negative Eu/Eu* anomaly (0.08–0.37).

Table 4 - Selected Trace and REE elements of garnets and zircon from leucosomes as obtained through in situ LA-ICPMS analyses and corresponding Zircon/Garnet REEs distribution coefficients (D_{REE})

Sample	K3L - MA09/28L - MA09/30L		K3L				K3L		MA09/28L		MA09/30L		Average	
Mineral	Zircon		Grt-2 cores		Grt-2 rim		Grt-3							
	Average (n=22)	Range	Average (n=6)	Range	Average (n=9)	Range	Average (n=14)	Range	Average (n=3)	Range	Average (n=5)	Range	Average (n=22)	Range
REE elements (ppm)														
La	0.09	*0-1.02*	0.01	*0-0.02*	0.04	*0-0.11*	0.35	*0.03-2.39*	0.12	*0.05-0.16*	0.02	*0.01-0.03*	0.27	*0.01-2.39*
Ce	1.21	*0.29-3.39*	0.11	*0.03-0.31*	0.22	*0.12-0.33*	0.84	*0.28-3.84*	0.35	*0.18-0.45*	0.10	*0.05-0.16*	0.61	*0.05-3.84*
Pr	0.05	*0.01-0.18*	0.11	*0.02-0.28*	0.22	*0.13-0.33*	0.28	*0.16-0.49*	0.10	*0.06-0.13*	0.12	*0.05-0.24*	0.22	*0.05-0.49*
Nd	1.11	*0.42-3.06*	2.60	*0.48-7.6*	5.36	*2.67-9.2*	5.73	*3.31-8.64*	1.63	*1.48-1.8*	4.25	*1.79-7.38*	4.83	*1.48-8.64*
Sm	4.49	*1.74-8.56*	5.11	*1.47-17.31*	10.65	*3.98-18.98*	18.67	*13.91-24.69*	7.34	*7.27-7.43*	13.36	*6.29-21.47*	15.92	*6.29-24.69*
Eu	0.28	*0.07-0.38*	0.54	*0.25-1.45*	0.89	*0.46-1.42*	1.11	*0.65-1.62*	0.97	*0.86-1.1*	1.37	*0.58-2.92*	1.15	*0.58-2.92*
Gd	36.38	*12.48-48.1*	19.63	*14.24-29.57*	20.42	*12.83-31.46*	43.04	*28-52*	30.94	*30.26-32.15*	33.94	*26.84-39.12*	39.32	*26.84-52*
Tb	14.18	*4.41-19.48*	8.58	*6.03-11.24*	6.51	*5.12-9.45*	6.71	*4.63-8.26*	6.00	*5.42-6.63*	6.70	*2.95-8.78*	6.61	*2.95-8.78*
Dy	140.57	*45.05-178.02*	142.26	*129.88-168.64*	53.62	*25.02-76.25*	30.41	*18.03-41.36*	27.39	*21.33-33.65*	39.23	*11.77-57.83*	32.00	*11.77-57.83*
Ho	42.07	*14.66-56.68*	57.36	*29.33-72.38*	10.66	*4.58-18.77*	4.12	*2.17-6.94*	3.68	*2.52-4.8*	6.74	*1.83-11.59*	4.65	*1.83-11.59*
Er	188.00	*69.05-277.14*	271.11	*113.14-342.46*	23.52	*8.74-50.72*	8.25	*4.07-17.61*	7.37	*4.1-10.59*	17.98	*4.27-32.51*	10.34	*4.07-32.51*
Tm	38.11	*14.81-57.38*	53.11	*21.33-69.96*	2.77	*0.89-5.93*	0.80	*0.39-2.22*	0.80	*0.32-1.27*	2.26	*0.53-3.83*	1.13	*0.32-3.83*
Yb	369.68	*148.87-543.59*	411.99	*191.61-593.51*	17.13	*5.33-39.43*	4.46	*1.87-11.71*	4.85	*2.98-7.29*	15.69	*3.87-26.71*	7.07	*1.87-26.71*
Lu	64.75	*25.83-100.62*	69.03	*36.68-94.42*	2.17	*0.65-4.22*	0.51	*0.2-1.23*	0.58	*0.29-0.98*	1.81	*0.43-3.06*	0.82	*0.2-3.06*
ΣLREE	2.44	*0.74-6.87*	2.83	*0.54-8.19*	5.84	*2.96-9.78*	7.20	*4.34-12.01*	2.20	*1.78-2.49*	4.48	*1.96-7.77*	5.90	*1.78-12.01*
ΣHREE	893.73	*335.16-1264.24*	1033.07	*552.19-1365.66*	136.80	*80.94-218.36*	98.29	*63.26-137.11*	81.60	*67.37-97.34*	124.35	*52.49-180.62*	101.94	*52.49-180.62*
$(La/Sm)_N$	0.01	*0-0.15*	0.002	*0-0.003*	0.003	*0-0.007*	0.12	*0.06-0.29*	0.19	*0.12-0.27*	0.53	*0.17-0.88*	0.01	*0.001-0.099*
$(Yb/Gd)_N$			26.94	*8.75-38.02*	1.12	*0.42-2.85*	5.23	*2.36-7.7*	4.05	*3.09-4.79*	1.88	*1.17-2.88*	0.22	*0.06-0.88*
$(Dy/Yb)_N$	0.27	*0.19-0.38*												
Eu/Eu*	0.07	*0.05-0.11*	0.17	*0.12-0.20*	0.19	*0.09-0.27*	0.12	*0.08-0.20*	0.20	*0.18-0.22*	0.19	*0.13-0.37*	0.15	*0.08-0.37*
Ti	5.31	*3.38-13.81*												
T °C [± 70 °C]*	684	*654-770*												
$D_{REE\ zircon/Grt}$														
La			9.92	*6.11-28.36*	2.30	*0.84-22.63*	0.27	*0.04-3.72*	0.76	*0.57-1.76*	6.09	*3.27-15.7*	0.33	*0.04-15.70*
Ce			11.16	*3.95-37.05*	5.37	*3.62-9.86*	1.43	*0.31-4.34*	3.41	*2.70-6.60*	12.21	*7.55-25.94*	1.90	*0.31-25.94*
Pr			0.47	*0.18-2.94*	0.24	*0.16-0.41*	0.19	*0.11-0.32*	0.53	*0.41-0.83*	0.42	*0.22-1.00*	0.24	*0.11-1.00*
Nd			0.43	*0.15-2.29*	0.21	*0.12-0.42*	0.19	*0.13-0.33*	0.68	*0.62-0.75*	0.26	*0.15-0.62*	0.23	*0.13-0.75*
Sm			0.88	*0.26-3.05*	0.42	*0.24-1.13*	0.24	*0.18-0.32*	0.61	*0.60-0.62*	0.34	*0.21-0.71*	0.29	*0.18-0.71*
Eu			0.52	*0.20-1.11*	0.32	*0.20-0.62*	0.25	*0.17-0.43*	0.29	*0.26-0.33*	0.21	*0.1-0.49*	0.25	*0.1-0.49*
Gd			1.85	*1.23-2.55*	1.78	*1.16-2.84*	0.85	*0.70-1.30*	1.18	*1.13-1.20*	1.07	*0.93-1.36*	0.94	*0.70-1.36*
Tb			1.65	*1.26-2.35*	2.18	*1.50-2.77*	2.11	*1.72-3.06*	2.36	*2.14-2.62*	2.11	*1.61-4.80*	2.16	*1.61-4.80*
Dy			0.99	*0.83-1.08*	2.62	*1.84-5.62*	4.62	*3.40-7.80*	5.13	*4.18-6.59*	3.58	*2.43-11.95*	4.41	*2.43-11.95*
Ho			0.73	*0.58-1.43*	3.95	*2.24-9.19*	10.22	*6.06-19.39*	11.45	*8.77-16.68*	6.24	*3.63-22.96*	8.99	*3.63-22.96*
Er			0.69	*0.55-1.66*	7.99	*3.71-21.51*	22.79	*10.67-46.17*	25.51	*17.76-45.83*	10.45	*5.78-44.05*	17.98	*5.78-46.17*
Tm			0.72	*0.54-1.79*	13.76	*6.43-42.62*	47.71	*17.2-97.77*	47.88	*30.01-118.31*	16.89	*9.96-71.33*	33.07	*9.96-118.31*
Yb			0.90	*0.62-1.93*	21.58	*9.38-65.38*	82.87	*31.57-198.07*	76.30	*50.71-123.98*	23.56	*13.84-95.56*	51.26	*13.84-198.07*
Lu			0.94	*0.69-1.77*	29.80	*15.34-100.04*	127.30	*52.7-325.73*	111.27	*66.27-225.52*	35.68	*21.15-149.37*	78.34	*21.15-325.73*

*Ti-in-zircon thermometry (Ferry and Watson, 2007).

10. Discussion

The structures in the field and the petrographic evidence presented in this study provide evidence of granulite-facies migmatisation of the immediate crustal envelope of the Beni Bousera peridotites. The presence of modally abundant garnet invariably characterises the mineral textures of both the melt segregates and melanosomes. In particular, the systematic spatial association of restitic garnet with leucosome segregations (Figs. 3e,f and 4a) is suggestive of incongruent melting and peritectic garnet growth (Brown, 2013) during crustal anatexis in the immediate envelope of the Beni Bousera peridotites. This is compatible with the presence of multiphase mineral inclusions of overall granitic compositions (Qz-Pl-Kfs ± Als) with lobate shapes and low-angle termination hosted in Grt-1 and Grt-2 grains (Fig. 4a–d), which can be interpreted as melt inclusions (Cesare et al., 2015), similarly to what already recognised for the migmatitic granulites of the Jubrique unit in the envelope of the Ronda peridotites of the Betic Cordillera (Barich et al., 2014; Acosta-Vigil et al., 2016). The evidence of high Ti and high Mg# Bt inclusion in Grt-1 outer rims surrounded by Pl-Kfsp-Qz aggregates supports a scenario of in situ dehydration melting of biotite and garnet growth according to the following general reaction (Patiño Douce and Johnston, 1991; Vielzeuf and Montel, 1994):

Bt + Als + Qz þ Pl➔Grt + Kfs + Melt (1)

Accordingly, the peak metamorphic assemblage is assumed to be constituted by the anhydrous assemblage made of Grt + Fsp + Qz

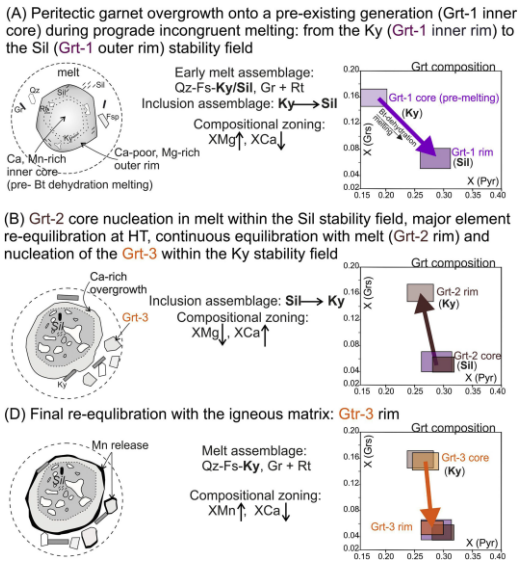

Fig. 11. Conceptual evolutionary model for the textural and compositional characteristics of the different garnet types recognised in the Beni Bousera migmatititic granulites.

+ Rt ± Als that was associated with melt. The pre-melting metamorphic evolution in the crustal envelope of the Beni Bousera peridotites is dominantly recorded by the Ca-rich and Mg-poor Grt-1 inner cores that are surrounded by the low (patchy zoned) Ca- and Mg-rich rim domains. Remnants of the melt(s) produced at the peak stage are preserved

in the Grt-1 rim and Grt-2 growth domains as composite mineral/melt inclusions (Qz-Fsp-Als), which document prograde melting, startedwithin the Ky stability field and continued to the Sil stability as recorded by the inner-to-outer rim inclusion assemblages in Grt-1. The Ca-poor and Mg-rich growth domains of Grt-1 rim compositions are thus interpreted as peritectic crystallisation products of prograde incongruent melting. Incipient crystallisation of the melt in the stability field of sillimanite is documented by Grt-2 cores. (Fig. 11a,b) Progressive crystallisation and cooling of the melt resulted in the formation of Ca-rich,Mg-poorer Grt-2 outer rims and Grt-3 grains during continuous cooling within the Ky stability field (Fig. 11c).

The post-peak retrograde evolution is attested by garnet resorption, Mn increase in garnet, and complex symplectic intergrown of Crd-Qz-Pl-Sp (Fig. 4i). The symplectite formation can be framed in a scenario of retrograde melt consuming reactions (e.g., White and Powell, 2002), controlled by reactions such as (e.g., Cai et al., 2017):

Grt + Als + Melt➔Crd + Bt + Fe–oxide (2)

The formation of texturally late Bt-Sil ± Ms. aggregates around garnet can be explained as a consequence of the reversal of reaction (1).

The almost complete preservation of the garnet porphyroblasts in the leucosomes and the relatively minor replacement of garnet in the melanosome, also suggests that significant hydrous melt extraction occurred after rocks anatexis in the envelope of the Beni Bousera peridotites. In fact, in migmatitic granulites where no melt loss occurred, the replacement of the anhydrous peritectic assemblage by hydrous phases (such as muscovite and biotite) in consequence of retrograde meltresiduum chemical interactions is expected (White and Powell, 2002). In this view, the melanosome is interpreted as the residuum produced by the passive accumulation of garnet after partial melting and extraction of a significant amount of melt.

10.1. Crustal anatexis: inverse thermobarometry

The P-T conditions attained during crustal anatexis are constrained through inverse thermobarometry as derived from the inclusion assemblages hosted in the peritectic Grt-1 rim and Grt-2 core growth domains, by coupling (i) the P-dependent Zr-in-rutile thermometry of Tomkins et al. (2007), combined with (ii) the Grt–Pl–Qz–Als (GASP) barometry (Ghent, 1976) as calculated with the THERMOCALC software v.3.33 (Powell et al., 1998).

The composition of the Rt grains found in different textural positions (as inclusion in Grt-1 (rims) and Grt-2 (cores and rims) and in the Qz-Fsp leucosome portions, respectively) were investigated through EMPA. The Rt inclusions in garnet yielded Zr contents ranging 1975–8827 ppm (n = 29), which provided temperatures ranging 776–1015 ± 40 °C (analytical uncertainty) at 0.8 GPa and 826–1076 ± 40 °C at 1.7 GPa, respectively. The corresponding lower and upper limits of the interquartile range values (Tomkins et al., 2007; Taylor-Jones and Powell, 2015) are 799–887 and 850–921 °C with a median value of 844±40 °C and 898±42 °C, respectively (see Supplementary Material 3). The Rt grains in the leucosome portions provided lower Zr contents, ranging 888–2053 ppm(n=64), resulting in temperature estimates of 741–833±40 °C at 0.8 GPa and 789–886±40 °C at 1.7 GPa. The corresponding lower and upper limits of the interquartile range values are 774–812 and 823–863 with a median value of 794 ± 19 and 845 ± 19 °C, respectively (see Supplementary Material 3).

The GASP equilibria were calculated using the Grt-1 rim (Grt-2 core) composition (X_{Grs}=0.07–0.09), combined with the Pl (X_{An}=35–45%) inclusion, setting the Qz and Sil (stable at the Grt-1 rim) activity to unit. The GASP barometry provided pressure estimates ranging from ca. 1.0 ± 0.1 GPa at 800 °C to 1.3 ± 0.1 GPa at 1000 °C.

The results from inverse thermo-barometry show that the minimum peak P-T conditions associated with melt segregation in the granulite envelope of the Beni Bousera peridotites are ca. 900–950 °C at 1.1–1.3 GPa, across the transition from the Ky (Grt-1 core) to the Sil (Grt-1 rim) stability (Fig. 12). These estimates are compatible with the results of melting experiments on pelitic compositions, which indicate that biotite is fully consumed by reaction (1) at temperature in the range 850–870 °C and garnet is the Fe-Mg peritectic phase produced at high-pressure (≥ 1.0 GPa) conditions (see reviews in Weinberg and Hasalová, 2015; Gao et al., 2016). The post-peak, retrograde assemblage made of Crd-Qz-Pl-Sp-Bt-Sil ± Ms. indicates decompressional cooling and constrains the final retrograde re-equilibration within the Crd stability field, below to ca. 0.5 GPa (e.g. White and Powell, 2011) (Fig. 12).

10.2. The path to crustal anatexis: Forward modelling

To refine the thermobaric evolution leading to crustal anatexis and magma production in the granulite envelope of the Beni Bousera peridotites, we adopted a single-step melt re-integration approach (e.g. Bartoli, 2017) by (i) estimating the relative fraction (vol%) of melt and residue at the outcrop scale (see Supplementary Material 4); and (ii) re-integrating the measured bulk average composition of leucosomes to that of a representative melanosome residue (Table 2). The resulting bulk composition as derived by using a 45 vol% of melt composition is assumed as the pre-melt bulk composition that is used for forward modelling thermobarometry using the software program PERPLEX (Connolly, 2005). The model system MnNCaKFMASTH (MnO–Na_2O–CaO–K_2O–FeO–MgO–Al_2O_3–SiO_2–TiO_2-H_2O) was chosen. The Fe_2O_3 was not

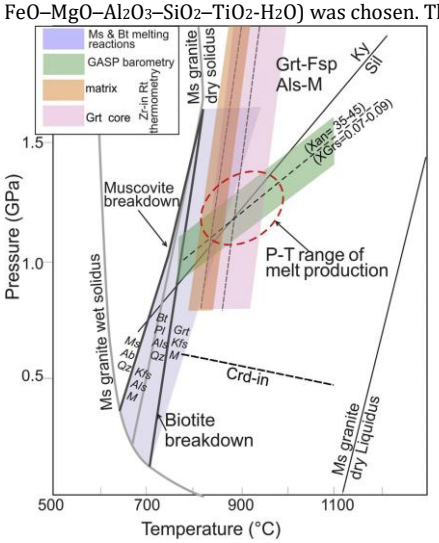

Fig. 12. Pressure-Temperature diagram showing the thermo-baric conditions attained during crustal anatexis in the Beni Bousera granulites as derived from inverse thermobarometry. The P-T grid and the relevant mineral and melting reactions are after Kotková and Harley (2010) and references therein.

considered in the model system, due to the presence of graphite in the mineral assemblage that is indicative of a reducing environment. The analysed loss of ignition (LOI) was assumed as H_2O. The following solidsolution models were used (details in the file solution.dat enclosed in the Perple_X package; database: hp04ver.dat, an updated version of the Holland and Powell (1998) thermodynamic dataset; Perple_X_6.8.7 version, downloaded July 27 2019): Grt(WPH) for garnet, Mica (CGH) for white mica, Bio(TCC) for biotite, Omph(GHP) for clinopyroxene, Pl (h) for plagioclase, San for K-feldspar and melt (HP) for the melt phase. Additional end-member phases considered in the calculations comprise quartz, rutile, ilmenite, kyanite and sillimanite. The pseudosections were constructed between 0.8 and 1.7 GPa and from 500 to 1100 °C.
These calculations are to be considered as tentative, for the uncertainty on (i) the starting bulk composition and proportion of melt loss, and (ii) the water content during progress of the metamorphism and crustalmelting.Moreover, since themodal content of retrogressive biotite in themelt products is very limited (ca 1% vol.), escape ofwater-rich melt has likely occurred, with a consequent bias in the melt reintegration procedure (e.g. Bartoli, 2017).
The output of the pseudosection modelling is shown in Fig. 13. The isopleth plots of the core-to-rim compositions as measured from garnet grains in the melanosome (Grt-1), combined with the hosted inclusion assemblages are used as a proxy of the thermobaric evolution during granulitisation and anatexis. Using the relevant Ca zoning in conjunction with the Mg content, the Grt-1 core compositions (X_{Grs} = 0.15–0.16, XPy=0.15–016) constrains the pre-melting prograde metamorphic evolution at ca. 550–600 °C and 1.3 GPa. These thermobaric estimates are well below the temperature conditions compatible with muscovite- and/or biotite-dehydration melting (800–850 °C in the relevant pressure range) and compatible with the biotite stability field, which limits peak pressure to 1.5–1.6 GPa (Fig. 13). Taking into account the abrupt rimward X_{Grs} decrease and X_{Pyr} increase (to 0.05–006 and to 0.30–0.31, respectively), combined with the evidence of transition from Ky to Sil inclusion from outer core to rim in Grt-1 (Fig. 4g), a nearly isothermal heating path is proposed. Peak conditions are therefore attained within the Sil stability field for temperatures of 950–1000 °C (Fig. 13). The transition to Ca-richer (up to 0.10) outer rim domains in some Grt-2 garnets, coupled with the leucosome mineralogy

documenting Ky as the stable Al_2SiO_5 polymorph in melt segregates (Qz-Fsp-Grt-Ky + Rt + Gr), provide evidence of nearly isothermal cooling within the Ky stability field during progressive crystallisation of the melt as monitored by the GASP reaction An = Grs + Ky + Qz. The absence of retrograde Bt in most of the leucosomes constrains the minimum P-T conditions of final melt crystallisation at ca. 1.1–1.2 GPa and 850–900 °C. The presence of lately formed Sil after Ky in the leucosomes, coupled with the Ca-poor rim composition of Grt-3 at a constant or even slightly increasing Mg content (Fig. 5d) impose a nearly isothermal exhumation path at a temperature of ca. 800 °C (Fig. 13).

To sum up, integration of inverse and forward modelling thermobarometry (Figs. 12, 13) suggests that melt production in the envelope of the Beni Bousera peridotites occurred at HP-(U)HT conditions with peak temperatures ɴ950 °C and crustal depths of ca. 50 km(assuming a rock density of 2800 kg/m3 at 1.3 GPa), followed by a nearly isobaric cooling at HP conditions (ca. 1.1–1.2 GPa and 800–850 °C). Despite the different peak temperature conditions, this scenario confirms what proposed for the granulites from Jubrique in the Betics, where the presence of melt at peak HP conditions has been also documented (Barich et al., 2014), but contrasts with the scenario of decompressional melting as earlier proposed both for the Ronda (Argles et al., 1999; Platt et al. (2003a) and the Beni Bousera (Álvarez-Valero et al., 2014) envelopes.

It is worth noting that the peak temperatures reconstructed in this study as derived from both inverse (Zr-in-Rt thermometry) and forward thermobarometry (likely ɴ900–950 °C) are not compatible with the Tiin-zircon thermometry, which provided lower temperatures (ca. 654–770 °C; Table 4). This is in accordance with the previous studies of HT and UHT migmatites, where the Zr-in-Rt thermometry has been documented to be more robust than the Ti-in-zircon in retaining the peak

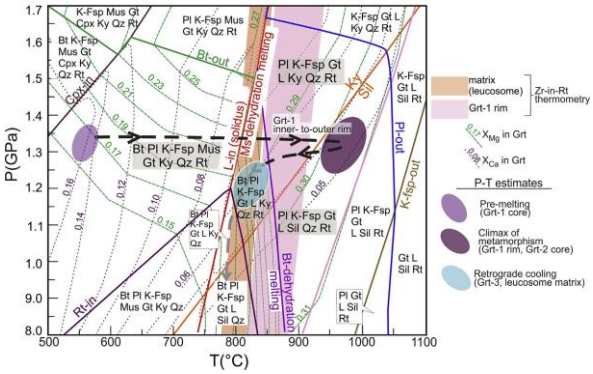

Fig. 13. Representative P-T pseudosection calculated for the reconstructed bulk rock composition (pre-melting) assuming a 45 45 vol% ofmelt loss in the systemMnNKCFMASHT (MnONa2O-K2O-CaO-FeO-MgO-Al2O3-SiO2-H2O-TiO2) with a bulk composition (wt%) MnO = 0.27, Na2O = 1.54, K2O = 4.19, FeO= 9.15, MgO = 2.44, Al2O3=22.98, SiO2=55.43,H2O= 1.46, TiO2 = 0.86, using the Perple_X software. The coloured ellipses indicate the main metamorphic stages as recorded by the inner crustal envelope of the Beni Bousera peridotites. The dashed lines and arrows depict (i) the inferred P-T path to the biotite dehydration melting as constrained from the X_{Grs} and X_{Pyr} isopleths in Grt-1 (core and rim) and Grt-2 (core) garnets; and (ii) the cooling path in the transition from the sillimanite to the kyanite stability field (Grt-2 rim and Grt-3 garnet composition).

metamorphic conditions (Bin Fu et al., 2008; Clark et al., 2009; Ewing et al., 2013). The convergence of the two thermometers requires the buffering assemblage of zircon-rutile-quartz (Watson et al., 2006; Taylor-Jones and Powell, 2015). In our samples, (i) the rutile grains found in the inclusion assemblage of the peritectic and igneous garnets (Grt-1 and Grt-2) only occur in equilibrium with quartz and not with zircon; (ii) zircon is instead dominantly observed in the matrix assemblages representing the final melt crystallisation. However, as discussed below, there are good arguments suggesting that zircon was present at peak temperature as represented by the Grt-1 outer rim/Gtr-2 core domains crystallisation.

10.3. Zircon-garnet-melt equilibria and the age of crustal anatexis

In high-grade environments as the one documented in this study, garnet and zircon are the primary competitors in controlling the MREE and HREE (from Sm to Lu) budget. In particular, the REE partitioning between zircon and garnet has become an essential tool to decipher the history of crustal anatexis and to link the U-Pb geochronology to the metamorphic evolution (e.g., Hokada and Harley, 2004; Clark et al., 2009; Hermann and Rubatto, 2003; Rocha et al., 2017; Rubatto, 2002; Rubatto and Hermann, 2007; Taylor et al., 2015, 2017; Villaros et al., 2009; Whitehouse and Platt, 2003).

The REE contents of the different garnet growth domains during melt crystallisation (Grt-2 and Grt-3) can be thus compared to those of the zircon and themelts products in order to better elucidate a possible

timing of zircon growth with respect to the leucosome production, crystallisation and cooling.

In order to verify equilibria between zircon and the two different suprasolidus (igneous) garnet populations, zircon/garnet ($D_{REE}^{Zrn/Grt}$) REEs distribution coefficients were calculated from the analysed material. Due to the homogeneous REE abundances in zircons (Fig. 10a), an average zircon composition was compared to those of the different garnet generations. Results are reported in Table 4 and shown in Fig. 14, where $D_{REE}^{Zrn/Grt}$ are compared with those experimentally determined for silicate melts at 900–1000 °C and 0.7 GPa (Taylor et al., 2015) and 800–1000 °C and 2.0 GPa (Rubatto and Hermann, 2007), conditions that are relevant for this study.

The elevated negative Eu anomalies in both zircon and garnet (Fig. 10) is mirrored by a strong positive Eu anomaly in the leucosomes (Fig. 7), which together indicate that zircons and garnet crystallised in equilibrium with plagioclase-bearing melts (e.g., Rubatto, 2002; Hoskin and Schaltegger, 2003). Significantly, the melanosomes show neutral to negative Eu anomaly, suggesting a fractionation process involving extraction of the Eu-rich phases from melanosome to leucosome (Fig. 7). This is in line with the major element composition of the in situ melt segregates (leucosomes), which are slightly Kdepleted and enriched in Ca/(Ca + Na) with respect to experimental melts (Fig. 6c,d), suggesting disequilibrium melting of plagioclase in the source and melt loss from the sites of melt accumulation (Sánchez-Navas et al., 2014; Taylor et al., 2014).

Significantly, the $D_{REE}^{Zrn/Grt}$ for the Grt-2 cores show nearly flat patterns for the HREE (from Dy to Lu), with the $D_{REE}^{Zrn/Grt}$ values varying close to the unity (Fig. 14; Table 4). These patterns are overlapping with the experimental data of Taylor et al. (2015) and Rubatto and Hermann (2007) at HT (1000 °C) (Fig. 14). In contrast, Grt-2 rims and Grt-3 show a significant increase of the HREE partitioning to zircon (Fig. 14; Table 4), essentially resulting from the HREE poor Grt-2 rim and Grt-3 compositions (Fig. 10b). This suggests an impoverishment of HREE in the remaining melt after major zircon crystallisation simultaneously or shortly after Grt-2 core growth. It is therefore suggested that the analysed zircons crystallised at nearly equilibrium conditions with the Grt-2 core throughout the cooling history of the segregated melts. We can thus propose an origin from the same melt/silicate system for both zircon and garnet sampled in the melt segregates from the inner granulite envelope of the Beni Bousera peridotites, in a scenario of prograde incongruent melting at high-pressure, melt production, extraction, crystallisation and cooling.

The internal structures (Fig. 8), together with the steep HREE patterns (Fig. 10a) of the zircons recovered from the leucosomes are compatible with this reconstruction, being indicative of crystallisation from a melt (e.g. Harley et al., 2007). The U\\Pb geochronology on euhedral and oscillatory to sector zoned growth domains constrains the partial melting event to Hercynian times (300–290 Ma) (Fig. 8). The low Th/U values obtained from the Hercynian igneous domains of the studied samples (Fig. 9) is compatible with the presence of monazite (Th-rich phase; e.g. Rubatto et al., 2013) during zircon growth and progress of rock anatexis in the crustal envelope of the Beni Bousera peridotites (Montel et al., 2000).

The few Cenozoic (ca. 20Ma) U-Pb zircon ages derived from the low Th/U (typically b0.01), structureless rims in zircons from the sample K3L (Fig. 8a) are instead compatible with metamorphic overgrowth. We refer this overgrowth stage to the low-pressure Alpine metamorphic/metasomatic event already documented in the inner envelope of the Beni Bousera peridotites, associated with a renewed episode of crustal anatexis and acidic magmatism, early Miocene in age (Rossetti et al., 2010, 2013). Similarly, an Alpine-aged recrystallisation and Pb loss event in the Hercynian zircons has been proposed for the polymetamorphic high-grade basement units of the Alpujarride complex in the Betics (Acosta-Vigil et al., 2014; Sánchez-Navas et al., 2014, 2017).

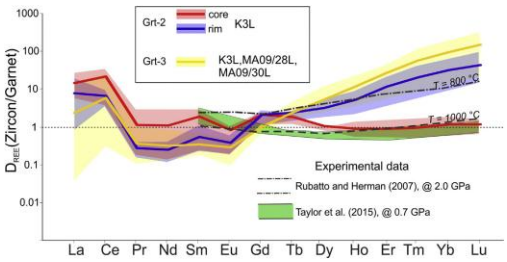

Fig. 14. Calculated zircon/garnets REE partitioning coefficients for the different samples compared with experimental data. The coloured fields display the whole range of values, the coloured continuos lines are the corresponding average values (see Table 4).

10.4. A Hercynian granulite-granite suite: Implications at regional scale

When integrated at the regional scale, the field, textural and geochronological data set discussed above may contribute to elucidate the P-T-t conditions and the petrological/geodynamic issues involved in the granulite-granite connection in the crustal section of the Alboran Domain.

The first significant result of our study is Hercynian HP/(U)HT granulite-facies migmatitic event is preserved in the core of the Alboran Domain of the Rif chain. Significantly, the crystallisation ages obtained from the melt segregates investigated in this study are, within error, the same as those obtained from the peraluminous HP (Grt-Ky-bearing) Hercynian granitoids (leptinites) that intrude the metamorphic core of the Alboran Domain of the Rif chain (Rossetti et al., 2010) (Fig. 9a). This evidence supports a scenario of HP/(U)HT Hercynian anatexis in the Beni Bousera envelope, synchronous with the segregation, crystallisation and emplacement of a suite of leucogranitic bodies in the supracrustal metamorphic sequence of the Filali unit.We therefore propose that a Hercynian granulite–granite suite is preserved in the Lower Sebtides nappe stack of the Moroccan Rif. In particular, the documented Hercynian granulite–granite suite can be coherently explained by a single metamorphic loop involving isobaric heating and cooling, followed by decompression, without the need to introduce a second (Alpine) major anatectic event in the high-grade basement of the Alboran Domain. This reconstruction is coherent with the isotopic data (Sr and Nd) available from both the Hercynian granitoids and the hosting granulite envelope of the Beni Bousera peridotites (Rossetti et al., 2013). The Hercynian granitoids show a relatively high $^{143}Nd/^{144}Nd$ values comparable with those of the coeval Iberian-French crustal magmas formed by the partial melting of metasedimentary protoliths that experienced a significant juvenile addition during the Cadomian events. Their origin by partial melting of the associated high-grade metamorphic rocks of the Beni Bousera units is thus isotopically consistent. The Alpine (early Miocene) crustal magmatism, being characterized by low $^{143}Nd/^{144}Nd$ values, is instead isotopically distinct from both the Hercynian granitoids and the granulite host rocks (Rossetti et al., 2013), thus attesting for a different metasedimentary source that is possibly identifiable in the metapelitic sequences drilled in the Alboran Basin (Comas et al., 1992).

Similar Hercynian ages are also derived from partial melting products in migmatitic units both at the footwall (Acosta-Vigil et al., 2014) and hanging wall (Ruiz Cruz and Sanz de Galdeano, 2014; Zeck and Williams, 2001; Zeck and Whitehouse, 2002; Sánchez-Navas et al., 2014, 2017; Gómez-Pugnaire, 2019) of the Ronda peridotites. Significant on this regard is the fact that the crustal melting fromthe granulite envelope of the Beni Bousera peridotites as reconstructed in this study is fully compatible, in terms of both textures and peak thermo-baric environments, with the HP anatectic history of the Jubrique unit at the hanging-wall of the Ronda peridotites (Barich et al., 2014; Acosta-Vigil et al., 2016). This evidence further confirms that partial melting in the envelope of the Alboran peridotites has occurred before the early Miocene Alpine decompressional evolution (e.g. Argles et al., 1999; Platt et al., 2003a). Moreover, the pre-Hercynian U-Pb zircon ages derived in this study from the high Th/U growth zoning domains (Fig. 9b,c) are also in agreement with those recovered from the high-grade migmatitic units of the Alpujarride-Septide realm (Acosta-Vigil et al., 2014; Melchiorre et al., 2017; Platt and Whitehouse, 1999; Rossetti et al., 2010; Sánchez-Navas et al., 2014; Zeck and Whitehouse, 2002; Zeck and Williams, 2001), suggesting a common crustal inheritance from wall-rock incorporation during the Hercynian anatectic event.

This reconstruction supports the presence of a Hercynian migmatised crustal domain in the metamorphic core of the Alboran Domain, structurally associated with the intracrustal emplacement of the Ronda and

Beni Bousera peridotite bodies.
The P-T evolution reconstructed for the migmatitic granulite envelope of the Beni Bousera peridotite documents a significant isobaric temperature increase (ca. 400 °C, from ca. 600 to ca. 1000 °C) and anatectic melt production at deep crustal conditions (ca. 1.3 GPa), during the Permo-Carboniferous transition from a subduction- (ca. 12 °C/km) to a Barrovian-type metamorphic gradient. This is followed by nearly isobaric cooling (ca. 150 °C) and a major isothermal decompression path (ca. 0.5 GPa at ca. 800 °C) during the final crystallisation history of the melt segregates (Fig. 13). This thermo-baric evolution implies a transient thermal input, followed by cooling and exhumation, compatible with a geodynamic scenario dominated by the convective removal of the deep roots of a mature orogen in a collisional setting (e.g., Dewey, 1988; Platt and England, 1994). The Beni Bousera units can be thus tentatively interpreted as fossil zone of crust-mantle coupling, developed after crustal thickening and intracrustal emplacement of hot peridotites bodies at convergent plate margins. Significantly, the late Carboniferous-early Permian ages documented in this study well fit with the late Carboniferous-early Permian tectono-magmatic events framed within the orogenic collapse stage of the Hercynian chain (e.g. Burg et al., 1994; Matte, 2001; Franke, 2006; Petri et al., 2017 and references therein). We can thus propose that the transition from the isobaric prograde/retrograde metamorphism to the isothermal exhumation in the Beni Bousera records the thermo-mechanical evolution of the deep roots of the Hercynian orogeny during the shift from crustal thickening to crustal thinning and collapse of the thermally weakened orogen (Molnar and Lyon-Caen, 1988; Platt and England, 1994; Vanderhaeghe, 2012).
Despite still debated are the peak pressure conditions attained by the high-grade crustal basement of the Alboran Domain (see Massonne et al., 2014), our results confirm previous estimates pointing to HP conditions for themetamorphic climax (Haissein et al., 2004; Bouybaouene et al., 1998) that we interpret as the evidence of a pre-Alpine (likely Hercynian in age) crustal thickening event preserved in the Lower Sebtides units of the Rif (e.g., Michard et al., 1997). Still unclear, however, is the linkage (if any) with the Hercynian UHP conditions proposed by Ruiz-Cruz and Sanz de Galdeano (2012, 2013) for the metamorphic evolution of the Lower Sebtides (Monte Hacho gneiss) exposed in the Ceuta region (Fig. 1).
The post-peak near-isothermal decompression led to the growth of a sequence of symplectitic reaction textures that record exhumation to higher crustal levels of the Beni Bousera units (within the cordierite stability field; below ca. 0.5 GPa; see also Acosta-Vigil et al., 2014). This final exhumation stage is geochronologically constrained during the Early Miocene (Rossetti et al., 2010; Melchiorre et al., 2017; this study), which corresponds to the main stage of the Alboran basin back-arc extension (Comas et al., 1999). Significantly, Early Miocene andalusite-bearing dyke swarms are intruded in the Beni-Bousera units, indicating the exhumation of the high-grade basement was almost already completed at that time (Rossetti et al., 2010, 2013).
Noteworthy are the implications of the above reconstruction for what concerns the impact of the Late Paleozoic template into the Alpine orogeny at a regional scale. First of all, the definitive demonstration of a polymetamorphic evolution of the high-grade basement of the Alboran Domain of the Western Mediterranean region is given (see also Acosta-Vigil et al., 2014; Sánchez-Navas et al., 2017), providing evidence that an important Hercynian tectono-metamorphic inheritance contributed to the structuration of the metamorphic core of the Betic-Rif orogen. In such a scenario, taking into account and re-interpreting the existing P-Tt data and tectonic/geodynamic reconstructions for the crust-mantle tectonic coupling in the Betic-Rif realm (e.g., Melchiorre et al., 2017; Hidas et al., 2013; Gueydan et al., 2015, 2019; Mazzoli and Martín-Algarra, 2011; Hidas et al., 2013; Frasca et al., 2017; Platt et al., 2003a, 2003b; Platt and Vissers, 1989; Garrido et al., 2011), it is possible to propose a tentative re-appraisal of the tectono-metamorphic evolution of the high-grade basement the Betic-Rif realm from Late Paleozoic onward, including insights on the intracrustal emplacement of the Ronda and Beni-Bousera mantle bodies. In particular, two main stages of crust-mantle coupling can be recognised in the region, that can be framed in Permo-Carboniferous and Neogene times, at deep and shallow crustal conditions, respectively.
The early stage occurred in the deep crust at the vanying stage of the Hercynian orogeny, associated with diffuse crustal anatexis and associated Granite magmatism (Fig. 15a,b). The Hercynian crust-mantle tectonic boundary then resided in the middle to shallow crustal conditions during the subsequent Early Mesozoic rifting phase associated with the formation

of the oceanic Tethyan realm (Melchiorre et al., 2017; Gimeno-Vives et al., 2019). During the Tertiary (Eocene), Alpine subduction and associated HP/LT metamorphism affected the Permo-Triassic supracrustal crustal rock units (upper Sebtides and Alpujarride complexes; Azañón et al., 1997, Bouybaouene et al., 1998; Michard et al., 2006), whereas the Hercynian basement largely escaped subduction and burial, being likely at the footwall of the main Alpine deformation front (Fig. 15c). Starting from the Neogene onward, the westward retreat of the Tethyan subduction caused back-arc extension, asthenosphere upwelling, lithosphere delamination and diffuse magmatism in the inner sectors of the chain, concurrently with the westward migration of the compressional fronts, thrusting the early structured and exhumed belt onto the external flysch domains (Royden et al., 1993; Frasca et al., 2017; Faccenna et al., 2004; Michard et al., 2006; Rossetti et al., 2013; Augier et al., 2005; Platt et al., 2013; Van Hinsbergen et al., 2014) (Fig. 15d). This corresponds to the final stage of intracrustal emplacement of the Ronda peridotites, commonly framed in a scenario of hot thrusting/transpression at shallow crustal conditions during switching from crustal extension to shortening in the upper plate domain of the Tethyan subduction (Pregicout et al., 2013; Garrido et al., 2011; Hidas et al., 2011; Frasca et al., 2017; Gueydan et al., 2019; Mazzoli and Martín-Algarra, 2011). The hypothesis of the two-stage (pre-Alpine and Alpine) crust-mantle coupling at different crustal depths in the Betic-Rif realm should be further validated through focused structural, petrological and geochronological investigations of the metamorphic envelopes of the Ronda and Beni Bousera peridotites.

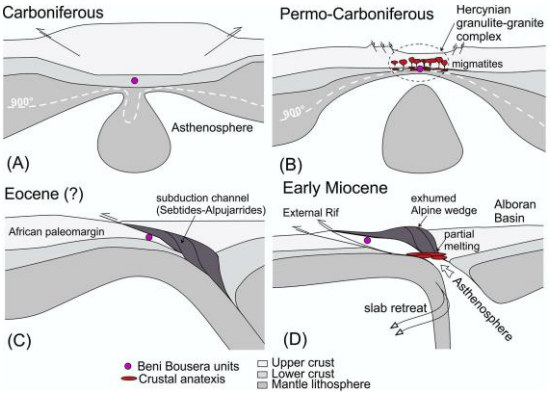

Fig. 15. Conceptual geodynamic evolutionary model for the tectono-metamorphic history of the Beni Bousera migmatitic granulites in the framework of the Betic-Rif tectonic realm.A two-stage (Permo-Carboniferous and Early Miocene) crust-mantle coupling is tentatively proposed (Not to scale; location of structures is only indicative).

On a wider scale, it is worth noting that the Hercynian (Permo-Carboniferous) signature detected from the granulite facies migmatitic envelopes of the Alboran peridotites is a common character of the pre-Alpine basement sections tectonically interleaved within the orogenic structure of the Alpine chain. In particular, similar temporal relationships between the Permo-Carboniferous granulite metamorphism and magmatism and are derived from the deep-crust/mantle transitions as exposed in the Ulten (Del Moro et al., 1999; Tumiati et al., 2003; Langone et al., 2011) and Ivrea-Verbano (e.g., Quick et al., 1995; Klötzli et al., 2014; Kunz et al., 2019; Guergouz et al., 2018) zones, Val Malenco (Herman et al., 1997; Hermann and Rubatto, 2003), Calabria (Graessner and Schenk, 2001) and the Northern Pyrenean Zone (Choukroune, 1992). This evidence is indicative of the complex growth of the continental crust across the Alpine realm through the multiple rifting-collisional events since detached from northern Gondwana paleo-margin (Early Paleozoic), assembled along the Hercynian belt, then fragmented/dispersed again during the Mesozoic, and finally reassembled and exhumed during the Alpine orogenic cycle (e.g. Stampfli and Borel, 2002). The spatial association of Hercynian and Alpine migmatitic complexes and crustal-derived granites across the Apine orogen is indicative of this complex geological history and stresses the importance of detailed petrographic, geochronological, geochemical and isotopic studies of the exposed high-grade crustal basement sections for the formulation of a consistent tectonometamorphic and geodynamic interpretation.

11. Conclusion

The main results derived from this study are as follow:

(i) A major Hercynian HP/(U)HT granulite-facies anatectic event associated

with the intracrustal emplacement of the Beni Bousera peridotites is documented;
(ii) A Hercynian granulite–granite suite is preserved in the Lower Sebtides nappe stack of the Alboran Domain of the Moroccan Rif;
(iii) A fossil Hercynian crust-mantle coupling zone is preserved at the core of the Alboran Domain, recording transition from orogenic construction to collapse;
(iv) The polymetamorphic nature of the high-grade basement of the Alboran Domain is confirmed, imposing the need to investigate further the P-T-t-deformation history associated with the crust-mantle coupling in the region;
(v) The crustal envelopes of the Alboran peridotites can be correlated to the pre-Alpine Permiam-Carboniferous lower crustal exposures exposed within the Alpine orogen of the Mediterranean region.
Results of this study impose a re-assessment of the metamorphic gradients, exhumation rates and thermo-baric environments associated with the Alpine construction of the Betic-Rif orogeny. In particular, when integrated with the available data from the Alboran Domain of the Betic chain our reconstruction fosters to re-consider the geodynamic significance of the Alpine high-grade tectono-metamorphic event in the Betic-Rif realm, including the models of the intracrustal emplacement of the Beni-Bousera and Ronda peridotites.

Supplementary data to this article can be found online at https://doi.org/10.1016/j.gr.2020.01.020.

Declaration of competing interest

The authors declare that they have no known competing financial interests or personal relationships that could have appeared to influence the work reported in this paper.

Acknowledgements

C. Faccenna, F. Tecce, D. Cozzupoli partecipated to the field work and are thanked for fruitful discussion and advice. N. Zaghloul is acknowledged for discussion and advice. H-J Massonne is thanked for discussion and for allowing access to the analytical facilities at the Institut für Mineralogie and Cristalchemie, Universität Stuttgart. M. Schmeltz is thanked for sample preparation. The Grant to Department of Science, Roma Tre University (MIUR-Italy Dipartimenti di Eccellenza, ARTICOLO 958 1, COMMI 314-337 LEGGE 232/2016) is gratefully acknowledged. This is FIERCE contribution No. 18. The constructive revision of L. Jolivet and A. Acosta Vigil contributed to improve significantly the manuscript.

References

Acosta-Vigil, A., Rubatto, D., Bartoli, O., Cesare, B., Meli, S., Pedrera, A., Azor, A., Tajčmanová, L., 2014. Age of anatexis in the crustal footwall of the Ronda peridotites, S Spain. Lithos 210–211, 147–167. https://doi.org/10.1016/j.lithos.2014.08.018.

Acosta-Vigil, A., Barich, A., Bartoli, O., Garrido, C.J., Cesare, B., Remusat, L., Poli, S., Raepsaet, C., 2016. The composition of nanogranitoids in migmatites overlying the Ronda peridotites (Betic Cordillera, S Spain): the anatectic history of a polymetamorphic basement. Contrib. Mineral. Petrol. 171. https://doi.org/10.1007/s00410-016-1230-3.

Álvarez-Valero, A.M., Jagoutz, O., Stanley, J., Manthei, C., ElMaz, A., Moukadiri, A., Piasecki, A., 2014. Crustal attenuation as a tracer for the emplacement of the Beni Bousera ultramafic massif (Betico-Rifean belt). Geol. Soc. Am Bulletin 126, 1614–1624. https://doi.org/10.1130/B31040.1.

Andriessen, P.A.M., Zeck, H.P., 1996. Fission-track constraints on timing of Alpine Nappe emplacement and rates of cooling and exhumation, Torrox area, Betic Cordilleras, S. Spain. Chem. Geol. 131, 199–206.

Andrieux, J., Fontbote, J.M.,Mattauer,M., 1971. Sur unmodèle explicatif de l'arc de Gibraltar. Earth Planet. Sci. Lett. 12, 191–198.

Argles, T.W., Platt, J.P.,Waters, D.J., 1999. Attenuation and excision of a crustal section during extensional exhumation: the Carratraca massif, Betic Cordillera, southern Spain. J. Geol. Soc. Lond. 156, 149–162. https://doi.org/10.1144/gsjgs.156.1.0149.

Augier, R., Agard, P., Moni, P., Jolivet, L., Robin, C., Booth-Rea, G., 2005. Exhumation, doming and slab retreat in the Betic Cordillera (SE Spain): in situ $^{40}Ar/^{39}Ar$ ages and P–T–d–t paths for the Nevado-Filabride complex. J. Metamorph. Geol. 23, 357–381. https://doi.org/10.1111/j.1525-1314.2005.00581.x.

Azañón, J.M., Crespo-Blanc, A., Garcıá-Dueñas, V., 1997. Continental collision, crustal thinning and nappe-forming during the pre-Miocene evolution of the Alpujarride complex (Alboran Domain, Betics). J. Struct. Geol. 19, 1055–1071.

Azdimousa, A., Bourgois, J., Poupeau, G., Vazquez, M., Asebriy, L., Labrin, E., 2014. Fission track thermochronology of the Beni Bousera peridotite massif (Internal Rif, Morocco) and the exhumation of ultramafic rocks in the Gibraltar Arc. Arab. J. Geosci. 7, 1993–2005.

Balanyá, J.C., Garcıá-Dueñas, V., Azañón, J.M., Sánchez-Gómez, M., 1997. Alternating contractional and extensional events in the Alpujarride nappes of the Alboran Domain (Betics, Gibraltar Arc). Tectonics 16, 226–238.

Barich, A., Acosta-Vigil, A., Garrido, C.J., Cesare, B., Tajčmanová, L., Bartoli, 2014. Microstructures and petrology of melt inclusions in the anatectic sequence of Jubrique (Betic Cordillera, S Spain): implications for crustal anatexis. Lithos 206–207, 303–320.

Bartoli, O., 2017. Phase equilibria modelling of residual migmatites and granulites: an

evaluation of the melt-reintegration approach. J. Metamorph. Geol. 2017 (35), 919–942. https://doi.org/10.1111/jmg.12261.
Bin Fu, F., Page, Z., Cavosie, A.J., Fournelle, J., Kita, N.T., Lackey, J.S.,Wilde, S.A., Valley, J.W., 2008. Ti-in-zircon thermometry: applications and limitations. Contrib. Mineral. Petrol. 156, 197–215.
Booth-Rea, G., Ranero, C.R., Martínez-Martínez, J.M., Grevemeyer, I., 2007. Crustal types and Tertiary tectonic evolution of the Alboran sea, westernMediterranean. Geochem. Geophys. Geosyst. 8. https://doi.org/10.1029/2007GC001639.
Bouybaouene, M.L., Michard, A., Goffé, B., 1998. High-pressure granulites on top of the Beni Bousera peridotites, Rif Belt, Morocco: a record of an ancient thickened crust in the Alboran domain. Bull. Soc. Géol. Fr. 169, 153–162.
Brown, M., 1994. The generation, segregation, ascent and emplacement of granite magma: themigmatite-to-crustally-derived granite connection in thickened orogens. Earth-Sci. Rev. 36, 83–130.
Brown, M., 2013. Granite: from genesis to emplacement. Geol. Soc. Am. Bull. 125, 1079–1113.
Burg, J.-P., Van Den Drissche, J., Brun, J.-P., 1994. Syn- to post-thickening extension in the Variscan Belt of western Europe: modes and structural consequences. Geologie de la France 3, 33–51.
Cai, J., Liu, F., Liu, P.,Wang, F., Liu, C., Shi, J., 2017. Anatectic record and P–T path evolution ofmetapelites fromthe Wulashan complex, Khondalite Belt, North China Craton. Precambrian Res. 303, 10–29.
Casciello, E., Fernàndez, M., Vergés, J., Montserrat, T., 2015. The Alboran Domain in the Western Mediterranean evolution: the birth of a concept. Bull. Soc. Geol. Fr. 186. https://doi.org/10.2113/gssgfbull.186.4-5.371.
Cesare, B., Acosta-Vigil, A., Bartoli, O., Ferrero, S., 2015. What can we learn from melt inclusions in migmatites and granulites? Lithos 239, 186–216.
Choukroune, P., 1992. Tectonic evolution of the Pyrenees. Annu. Rev. Earth Planet. Sci. 20, 143–158.
Clark, C., Collins, A.S., Santosh, M., Taylor, R.,Wade, B.P., 2009. The P-T-t architecture of a Gondwanan suture: REE, U–Pb and Ti-in-zircon thermometric constraints from the Palghat Cauvery shear system, south India. Precambrian Res. 174, 129–144.
Comas, M.C., Platt, J.P., Soto, J.I., Watts, A.B., 1999. The origin and tectonic history of the Alboran Basin: insights from Leg 161 results. Proc. Ocean Drill. Proj. Sci. Results 161, 555–579.
Connolly, J.A.D., 2005. Computation of phase equilibria by linear programming: a tool for geodynamic modeling and its application to subduction zone decarbonation. Earth Planet. Sci. Lett. 236, 524–541.
Corfu, F., Hanchar, J.M., Hoskin, P.W.O., Kinny, P., 2003. Atlas of Zircon Textures. Rev. Mineral. Geochem. 53, 469–500.
DelMoro, A.,Martin, S., Prosser, G., 1999. Migmatites of the Ulten zone (NE Italy), a record of melt transfer in deep crust. J. Petrol. 40, 1803–1826.
Dewey, J.F., 1988. Extensional collapse of orogens. Tectonics 7, 1123–1139. https://doi.org/10.1029/TC007i006p01123.
Dewey, J.F., Helman, M.L., Turco, E., Hutton, D.H.W., Knott, S.D., 1989. Kinematics of the western Mediterranean. In: Coward, M.P., Dietrich, D., Park, R.G. (Eds.), Alpine Tectonics. Geol. Soc. Spec. Publ. 45, pp. 421–443.
El Maz, A., Guiraud, M., 2001. Paragenese à faible variance dans les métapelites de la sèrie de Filali (Rif interne marocain): description, interpretation et conséquences géodynamiques. Bulletin de la Société Géologique de France 172, 469–485.
Esteban, J. J., Sánchez-Rodrıguez,, L., Seward, D., Cuevas, J., Tubía, J.M., 2004a. Late thermal history of the Ronda area, southern Spain. Tectonophysics 398, 81–92.
Esteban, J.J., Sánchez-Rodríguez, L., Seward, D., Cuevas, J., Tubía, J.M., 2004b. The late thermal history of the Ronda area, southern Spain. Tectonophysics 389, 81–92.
Esteban, J.J., Cuevas, J., Tubía, J.M., Liati, A., Seward, D., Gebauer, D., 2007. Timing and origin of zircon-bearing chlorite schists in the Ronda peridotites (Betic Cordilleras, Southern Spain). Lithos 99, 121–135.
Esteban, J.J., Cuevas, J., Tubía, J.M., Sergeev, S., Larionov, A., 2010. A revised Aquitanian age for the emplacement of the Ronda peridotites (Betic Cordilleras, southern Spain). Geol. Mag. 147. https://doi.org/10.1017/S0016756810000737.
Ewing, T.A., Hermann, J., Rubatto, D., 2013. The robustness of the Zr-in-rutile and Ti-inzircon thermometers during high-temperature metamorphism (Ivrea-Verbano Zone, northern Italy). Contrib. Mineral. Petrol. 165, 757–779.
Faccenna, C., Becker, T.W., Lucente, F.P., Rossetti, F., 2001. History of subduction and backarc extension in the central Mediterranean. Geophys. J. Int. 145, 1–21.
Faccenna, C., Piromallo, C., Crespo-Blanc, A., Jolivet, L., Rossetti, F., 2004. Lateral slab deformation and the origin of the western Mediterranean arcs. Tectonics 23, TC1012.
Franke, W., 2006. The Variscan orogen in Central Europe: construction and collapse. In: Gee, D.G., Stephenson, R.A. (Eds.), European Lithosphere Dynamics. Geological Society, London, Memoirs 32, pp. 333–343.
Frasca, G., Gueydan, F., Poujol, M., Brun, J.-P., Parat, F., Monié, P., et al., 2017. Fast switch from extensional exhumation to thrusting of the Ronda Peridotites (South Spain). Terra Nova 29, 117–126. https://doi.org/10.1111/ter.12255.
Gao, P., Zheng, Y.-F., Zhao, Z.-F., 2016. Experimental melts from crustal rocks: a lithochemical constraint on granite petrogenesis. Lithos 266–267, 133–157.
García-Casco, A., Torres-Roldán, R.L., 1999. Natural metastable reactions involving garnet, staurolite and cordierite: Implications for petrogenetic grids and the extensional collapse of the Betic-Rif Belt. Contrib. Mineral. Petrol. 136, 131–153. https://doi.org/10.1007/s004100050528.
24 F. Rossetti et al. / Gondwana Research 83 (2020) 157–182
García-Dueñas, V., Balanyá, J.C., Martínez-Martínez, J.M., 1992. Miocene extensional detachments in the outcropping basement of the northern Alboran Basin and their tectonic implications. Geo-Mar. Lett. 12, 88–95. https://doi.org/10.1007/BF02084917.
Garrido, C.J., Gueydan, F., Booth-Rea, G., Precigout, J., Hidas, K., Padron-Navarta, J.A., Marchesi, C., 2011. Garnet lherzolite and garnet-spinelmylonite in the Ronda peridotite: Vestiges of Oligocene backarcmantle lithospheric extension in thewestern Mediterranean. Geology 39, 927–930. https://doi.org/10.1130/G31760.1.
Ghent, E.D., 1976. Plagioclase-garnet-Al_2SiO_5-Quartz: a potential geobarometergeothermometer. Am. Mineral. 61, 710–714.
Gimeno-Vives, O., Mohn, G., Bosse, V., Haissen, F., Zaghloul, M.N., Atouabat, A., Frizon de Lamotte, D., 2019. The Mesozoic margin of the Maghrebian Tethys in the Rif belt

Morocco: evidence for polyphase rifting and related magmatic activity. Tectonics 38, 2894–2918. https://doi.org/10.1029/2019TC005508.
Gómez-Pugnaire,M.T., Nieto, F., Abad, I., Velilla, N., Garrido, C.J., Acosta-Vigil, A., Barich, A., Hidas, K., Lopez Sanchez-Vizcaino, V., 2019. Alpine metamorphism in the Betic internal zones. In: Quesada, C., Oliveira, J.T. (Eds.), The geology of Iberia: A geodynamic approach. Springer Nature, Switzerland, pp. 519–554. https://doi.org/10.1007/978-3-030-11295-0_13.
Graessner, T., Schenk, V., 2001. An exposed Hercynian deep crustal section in the Sila Massif of northern Calabria: mineral chemistry, petrology and a P–T path of granulite-facies metapelitic migmatites and metabasites. J. Petrol. 42, 931–961.
Guergouz, C., Martin, L., Vanderhaeghe, O., Thébaud, N., Fiorentini, M., 2018. Zircon and monazite petrochronologic record of prolonged amphibolite to granulite faciesmetamorphism in the Ivrea-Verbano and Strona-Ceneri zones, NW Italy. Lithos 308–309, 1–18.
Guerrera, F., Martín-Martín, M., Tramontana, M., 2019. Evolutionary geological models of the central-western peri-Mediterranean chains: a review. Int. Geol. Rev. https://doi.org/10.1080/00206814.2019.1706056.
Gueydan, F., Pitra, P., Afiri, A., Poujol, M., Essaifi, A., Paquette, J.-L., 2015. Oligo-Miocene thinning of the Beni Bousera peridotites and their Variscan crustal host rocks, Internal Rif, Morocco. Tectonics 34, 1244–1268. https://doi.org/10.1002/2014TC003769.
Gueydan, F., Mazzotti, S., Tiberi, C., Cavin, R., Villasenor, A., 2019.Western Mediterranean sub-continental mantle emplacement by continental margin obduction. Tectonics https://doi.org/10.1029/2018TC005058.
Harley, S.L., Kelly, N.M., Möller, A., 2007. Zircon behaviour and the thermal histories of mountain chains. Elements 3, 25–30. https://doi.org/10.2113/gselements.3.1.25.
Hermann, J., Rubatto, D., 2003. Relating zircon and monazite domains to garnet growth zones: age and duration of granulite facies metamorphism in the Val Malenco lower crust. J. Metamorph. Geol. 21, 833–852.
Hidas, K., Booth-Rea, G., Garrido, C.J., Martínez-Martínez, J.M., Padrón-Navarta, J.A., Konc, Z., Giaconia, F., Frets, E., Marchesi, C., 2013. Backarc basin inversion and subcontinentalmantle emplacement in the crust: kilometre-scale folding and shearing at the base of the proto-Alborán lithospheric mantle (Betic Cordillera, southern Spain). J. Geol. Soc. 170, 47–55. https://doi.org/10.1144/jgs2011-151.
Hokada, T., Harley, S.L., 2004. Zircon growth in UHT leucosome: constraints from zircon–garnet rare earth elements (REE) relations in Napier complex, East Antarctica. J. Mineral. Petrol. Sci. 99, 180–190.
Holland, T.J.B., Powell, R., 1998. An internally consistent thermodynamic data set for phases of petrological interest. J. Metamorph. Geol. 16, 309–343.
Homonnay, E., Corsini, M., Lardeaux, J.-M., Romagny, A., Münch, P., Bosch, D., Cenki-Tok, B., Ouazzani-Touhami, M., 2018. Miocene crustal extension following thrust tectonic in the lower Sebtides units (internal Rif, Ceuta Peninsula, Spain): Implication for the geodynamic evolution of the Alboran domain. Tectonophysics 722, 507–535. https://doi.org/10.1016/j.tecto.2017.11.028.
Hoskin, P.W.O., Schaltegger, U., 2003. The composition of zircon and igneous and metamorphic petrogenesis. In: Hanchar, J.M., Hoskin, P.W.O. (Eds.), Zircon, 53. Mineralogical Society of America, Reviews in Mineralogy & Geochemistry, Washington, DC, pp. 27–62.
Janots, E., Negro, F., Brunet, F., Goffè, B., Engi, M., Bouybaouene, M.L., 2006. Evolution of the REE mineralogy in HP-LT metapelites of the Sebtides complex, Rif, Morocco: Monazite stability and geochronology. Lithos 87, 214–234.
Jolivet, L., Faccenna, C., 2000. Mediterranean extension and the Africa-Eurasia collision. Tectonics 19, 1095–1106. https://doi.org/10.1029/2000TC900018.
Jolivet, L., Augier, R., Faccenna, C., Negro, F., Rimmele, G., Agard, P., Robin, C., Rossetti, F., Crespo-Blanc, A., 2008. Subduction, convergence and the mode of backarc extension in the Mediterranean region. Bull. Soc. Géol. Fr. 179, 525–550.
Klötzli, U.S., Sinigoi, S., Quick, J.E., Demarchi, G., Tassinari, C.C., Sato, K., Günes, Z., 2014. Duration of igneous activity in the Sesia Magmatic System and implications for hightemperature metamorphism in the Ivrea–Verbano deep crust. Lithos 206, 19–33.
Kornprobst, J., 1974. Contribution a l'ètude pètrographique et structurale de la zone interne du Rif (Maroc septentrional); Petrography and structure of the Rif inner area, northern Morocco. Notes Mèm. Serv. Gèol. Rabat 251 (256 pp).
Kotková, J., Harley, S.L., 2010. Anatexis during highpressure crustal metamorphism: evidence from garnet–whole-rock REE relationships and zircon–rutile Ti–Zr thermometry in leucogranulites from the Bohemian Massif. J. Petrol. 51, 1967–2001.
Kunz, B.E., Manzotti, P., von Niederhäusern, B., Engi, M., Darling, J.R., Giuntoli, F., Lanari, P., 2018. Permian high-temperaturemetamorphismin theWestern Alps (NWItaly). Int. J. Earth Sci. 107, 203–229. https://doi.org/10.1007/s00531-017-1485-6.
Langone, A., Braga, R., Massonne, H.J., Tiepolo, M., 2011. Preservation of old (prograde metamorphic) U–Th–Pb ages in unshielded monazite from the high-pressure paragneisses of the Variscan Ulten Zone (Italy). Lithos 127, 68–85.
Lonergan, L.,White, N., 1997. Origin of the Betic-Rif mountain belt. Tectonics 16, 504–522.
Ludwig, K., 2003. User's manual for Isoplot/Ex v3.0, a geochronological toolkit for Miscrosoft Excel. Spec. Publ. 4. Berkeley Geochronological Center, Berkeley, California, pp. 25–31.
Matte, P., 2001. The Variscan collage and orogeny (480-290 Ma) and the tectonic de®-nition of the Armorica microplate: a review. Terra Nova 13, 122–128.
Mazzoli, S.,Martín-Algarra, A., 2011. Deformation partitioning during transpressional emplacement of a 'mantle extrusion wedge': the Ronda peridotites, western Betic Cordillera. Spain. J. Geol. Soc. Lond. 168, 373–382.
Melchiorre, M., Álvarez-Valero, A.M., Vergés, J., Fernàndez, M., Belousova, E.A., El Maz, A., Moukadiri, A., 2017. In situ U-Pb zircon geochronology on metapelitic granulites of Beni Bousera (Betic-Rif system, N Morocco). In: Bianchini, G., Bodinier, J.-L., Braga, R., Wilson, M. (Eds.), The Crust-mantle and Lithosphere-asthenosphere Boundaries: Insights From Xenoliths, Orogenic Deep Sections, and Geophysical Studies: Geological Society of America Special Paper. 526, pp. 151–171. https://doi.org/10.1130/2017.2526(08.
Michard, A., Goffé, B., Bouybaouene, M.L., Saddiqi, O., 1997. Late Hercynian-Mesozoic thinning in the Alboran domain; metamorphic data from the northern Rif, Morocco. Terra Nova 9, 171–174. https://doi.org/10.1046/j.1365-3121.1997.d01-24.x.
Michard, A., Negro, F., Saddiqi, O., Bouybaouene, M.L., Chalouan, A., Montigny, R., Goffé, B., 2006. Pressure-temperature-time constraints on theMaghrebide mountain building: evidence from the Rif-Betic transect (Morocco, Spain), Algerian correlations, and

geodynamic implications. C. R. Acad. Sci., Ser. II 338, 92–114.
Molnar, P., Lyon-Caen, H., 1988. Some Physical Aspects of the Support, Structure, and Evolution of Mountain Belts. vol. 218. Special Papers of the Geological Society of America, pp. 179–207.
Monié, P., Torres Roldan, R.L., Garcià Casco, A., 1994. Cooling and exhumation of theWestern Betic Cordilleras, 40Ar/39Ar thermochronological constraints on a collapsed terrane. Tectonophysics 238, 353–379.
Montel, J.M., Kornprobst, J., Vielzeuf, D., 2000. Preservation of old U–Th–Pb ages in shielded monazite; example from the Beni Bousera Hercynian kinzigites (Morocco). J. Metamorph. Geol. 18, 335–342.
Negro, F., Beyssac, O., Goffé, B., Saddiqi, O., Bouybaouene, M.L., 2006. Thermal structure of the Alboran Domain in the Rif (northernMorocco) and theWestern Betics (southern Spain) constraints from Raman spectroscopy of carbonaceous material. J. Metamorph. Geol. 24, 309–327.
Patiño Douce, A.E., Johnston, A.D., 1991. Phase equilibria and melt productivity in the pelitic system: implications for the origin of peraluminous granitoids and aluminous granulites. Contrib. Mineral. Petrol. 107, 202–218.
Petri, B., Mohn, G., Skrzypek, E., Mateeva, T., Galster, F., Manatschal, G., 2017. U–Pb geochronology of the Sondalo gabbroic complex (Central Alps) and its position within the Permian post-Variscan extension. Int. J. Earth Sci. 106, 2873–2893.
Platt, J.P., England, P.C., 1994. Convective removal of lithosphere beneath mountain belts: thermal and mechanical consequences. Am. J. Sci. 294, 307–336.
Platt, J.P., Vissers, R.L.M., 1989. Extensional collapse of thickened continental lithosphere: a working hypothesis for the Alboran Sea and Gibraltar Arc. Geology 17, 540–543.
Platt, J.P., Whitehouse, M.J., 1999. Early Miocene high-temperature metamorphism and rapid exhumation in the Betic Cordillera (Spain): evidence from U–Pb zircon ages. Earth Planet. Sci. Lett. 171, 591–605.
Platt, J.P., Soto, J.I., Whitehouse, M.J., Hurford, A.J., Kelley, S.P., 1998. Thermal evolution, rate of exhumation, and tectonic significance of metamorphic rocks from the floor of the Alboran extensional basin, western Mediterranean. Tectonics 17, 671–689.
Platt, J.P., Argles, T.W., Carter, A., Kelley, S.P.,Whitehouse, M.J., Lonergan, L., 2003a. Exhumation of the Ronda peridotite and its crustal envelope: constraints from thermal modelling of a P–T–time array. J. Geol. Soc. Lond. 160, 655–676.
Platt, J.P., Whitehouse, M.J., Kelley, S.P., Carter, A., Hollick, L., 2003b. Simultaneous extensional exhumation across the Alboran Basin: implications for the causes of late orogenic extension. Geology 31, 251–254.
Platt, J.P., Kelley, S.P., Carter, A., Orozco, M., 2005. Timing of tectonic events in the Alpujárride complex, Betic Cordillera, southern Spain. J. Geol. Soc. Lond. 162, 451–462.
Platt, J.P., Behr,W.M., Johanesen, K.,Williams, J.R., 2013. The Betic-Rif Arc and its orogenic hinterland: a review. Annu. Rev. Earth Planet. Sci. 2013 (41), 14.1–14.45. https://doi.org/10.1146/annurev-earth-050212-123951.
Powell, R., Holland, T.J.B., 2008. On thermobarometry. J. Metamorph. Geol. 26, 155–179.
Powell, R., Holland, T.J.B.,Worley, B., 1998. Calculating phase diagrams involving solid solutions via non-linear equations, with examples using THERMOCALC. J. Metamorph. Geol. 16, 577–588.
Priem, H.N.A., Boelrijk, N.A.I.M., Hebeda, E.H., Verschure, R.H., 1966. Isotopic age determinations on tourmaline granite-gneisses and ametagranite in the eastern Betic Cordilleras (southeastern Sierra de los Filabres), SE Spain. Geol. Mijnb. 45, 184–187.
Priem, H.N.A., Boelrijk, N.A.I.M., Hebeda, E.H., Oen, I.S., Verdurmen, E.A.Th., Verschure, R.H., 1979. Isotopic dating of the emplacement of the ultramafic masses in the Serranía de Ronda, Southern Spain. Contrib. Mineral. Petrol. 70, 103–109.
Puga, E., Nieto, J.M., Diaz de Federico, A., Bodinier, J.L., Morten, L., 1999. Petrology and metamorphic evolution of ultramafic rocks and dolerite dykes of the Betic Ophiolite Association (Mulhacen complex, SE Spain): evidence of eo-Alpine subduction following an ocean-floor metasomatic process. Lithos 49, 23–56.
Quick, J.E., Sinigoi, S.,Mayer, A., 1995. Emplacement ofmantle peridotite in the lower continental crust, Ivrea-Verbano zone, northwest Italy. Geology 23, 739–742.
Rocha, B.C., Moraes, R.,Möller, A., Cioffi, C.R., Jercinovic,M.J., 2017. Timing of anatexis and melt crystallization in the Socorro–Guaxupé Nappe, SE Brazil: insights from trace element composition of zircon, monazite and garnet coupled to U—Pb geochronology. Lithos 277, 337–355.
Rossetti, F., Faccenna, C., Crespo-Blanc, A., 2005. Structural and kinematic constraints to the exhumation of the Alpujarride complex (Central Betic Cordillera, Spain). J. Struct. Geol. 27, 199–216. https://doi.org/10.1016/j.jsg.2004.10.008.
Rossetti, F., Theye, T., Lucci, F., Bouybaouene, M.L., Dini, A., Gerdes, A., Phillips, D., Cozzupoli, D., 2010. Timing and modes of granites magmatism in the core of the Alboran Domain, Rif Chain, northern Morocco: implications for the Alpine evolution
F. Rossetti et al. / Gondwana Research 83 (2020) 157–182 25
of the Western Mediterranean. Tectonics 29, TC2017. https://doi.org/10.1029/2009TC002487.
Rossetti, F., Dini, A., Lucci, F., Bouybaouene, M.L., Faccenna, C., 2013. Early Miocene strikeslip tectonics and granite emplacement in the Alboran Domain (Rif chain, Morocco): significance for the geodynamic evolution of westernMediterranean. Tectonophysics 608, 774–791.
Royden, L.H., 1993. Evolution of retreating subduction boundaries formed during continental collision. Tectonics 12, 629–638.
Rubatto, D., 2002. Zircon trace element geochemistry: distribution coefficients and the link between U–Pb ages and metamorphism. Chem. Geol. 184, 123–138.
Rubatto, D., Hermann, J., 2007. Experimental zircon/melt and zircon/garnet trace element partitioning and implications for the geochronology of crustal rocks. Chem. Geol. 241, 38–61.
Rubatto, D., Chakraborty, S., Dasgupta, S., 2013. Timescales of crustalmelting in the higher Himalayan Crystallines (Sikkim, Eastern Himalaya) inferred from trace element constrained monazite and zircon chronology. Contrib. Mineral. Petrol. 165, 349–372.
Ruiz Cruz, M.D., Sanz de Galdeano, C., 2014. Garnet variety and zircon ages in UHP metasedimentary rocks from the Jubrique zone (Alpujárride complex, Betic Cordillera, Spain): evidence for a pre-Alpine emplacement of the Ronda peridotite. Int. Geol. Rev. 56, 845–868.
Ruiz-Cruz, M.D., Sanz de Galdeano, C., 2012. Diamond and coesite in the ultrahighpressure–ultrahigh-temperature granulites from Ceuta, Northern Rif. Northwest

Africa Mineralogical Magazine 76 (2012), 683–705.
Ruiz-Cruz, M.D., Sanz de Galdeano, C., 2013. Coesite and diamond inclusions, exsolutions microstructures and chemical patterns in ultrahigh-pressure garnet from Ceuta (Northern Rif, Spain). Lithos 177, 184–206.
Sánchez-Navas, A., García-Casco, A., Martín-Algarra, A., 2014. Pre-Alpine discordant granitic dikes in the metamorphic core of the Betic Cordillera: tectonic implications. Terra Nova 26, 477–486.
Sánchez-Navas, A., García-Casco, A., Mazzoli, S., Martín-Algarra, A., 2017. Polymetamorphism in the Alpujarride complex, Betic Cordillera, South Spain. The Journal of Geology 125. https://doi.org/10.1086/693862.
Sánchez-Rodrıguez, L., Gebauer, D., 2000. Mesozoic formation of pyroxenites and gabbros in the Ronda area (southern Spain), followed by EarlyMiocene subduction metamorphism and emplacement into the middle crust: U-Pb sensitive high-resolution ion microprobe dating of zircon. Tectonophysics 316, 19–44.
Sawyer, E.W., 1994. Melt segregation in the continental crust. Geology 22, 1019–1022.
Sawyer, E.W., 2008. Atlas of migmatites. The Canadian Mineralogist. Special Publication, Vol. 9. NRC Research Press, Ottawa, Ontario, p. 371.
Schmid, S.M., Fügenschuh, B., Kissling, E., Schuster, R., 2004. Tectonic map and overall architecture of the Alpine orogen. Eclogae Geol. Helv. 97, 93–117.
Sosson, M., Morrillon, A.-C., Bourgois, J., Feraud, G., Poupeau, G., Saint-Marc, P., 1998. Late exhumation stages of the Alpujarride complex (western Betic Cordilleras, Spain): new thermochronological and structural data on Los Reales and Ojen nappes. Tectonophysics 285, 253–273.
Soto, J.I., Platt, J.P., 1999. Petrological and structural evolution of high-grademetamorphic rocks from the floor of the Alboran Sea basin, Western Mediterranean. J. Petrol. 40, 21–60.
Stampfli, G.M., Borel, G.D., 2002. A plate tectonic model for the Paleozoic and Mesozoic constrained by dynamic plate boundaries and restored synthetic oceanic isochrones. Earth Planet. Sci. Lett. 196, 17–33. https://doi.org/10.1016/S0012-821X(01)00588-X.
Sun, S.S., McDonough, W.S., 1989. Chemical and isotopic systematics of oceanic basalts: implications for mantle composition and processes. Geol. Soc. Lond., Spec. Publ. 42, 313–345.
Taylor, J., Nicoli, G., Stevens, G., Frei, D., Moyen, J.F., 2014. The processes that control leucosome compositions in metasedimentary granulites: perspectives from the Southern marginal Zone migmatites, Limpopo Belt, South Africa. J. Metamorph. Geol. 32, 713–742.
Taylor, R.J.M., Harley, S.L., Hinton, R.W., Elphick, S., Clark, C., Kelly, N.M., 2015. Experimental determination of REE partition coefficients between zircon, garnet andmelt: a key to understanding high-T crustal processes. J. Metamorph. Geol. 33, 231–248.
Taylor, R.J.M., Clark, C., Harley, S.L., Kylander-Clark, A.R.C., Hacker, B.R., Kinny, P.D., 2017. Interpreting granulite facies events through rare earth element partitioning arrays. J. Metamorph. Geol. 35, 759–775. https://doi.org/10.1111/jmg.12254.
Taylor-Jones, Powell, R., 2015. Interpreting zirconium-in-rutile thermometric results. J. Metamorph. Geol. 33, 115–122.
Tomkins, H.S., Powell, R., Ellis, D.J., 2007. The pressure dependence of the zirconium-inrutile thermometer. J. Metamorph. Geol. 25, 703–713.
Torres-Roldán, R.L., 1983. Fractionated melting of metapelite and further crystal-melt equillibria. The example of the Blanca Unit migmatite complex, north of Estepona (southern Spain). Tectonophysics 96, 95–123.
Tubía, J., Cuevas, J., 1986. High-temperature emplacement of the Los Reales Peridotite nappe (Betic Cordillera, Spain). J. Struct. Geol. 8, 473–482.
Tubía, J., Cuevas, J., Ibarguchi, J.G., 1997. Sequential development of the metamorphic aureole beneath the Ronda Peridotites and its bearing on the tectonic evolution of the Betic Cordillera. Tectonophysics 279, 227–252.
Tumiati, S., Thöni,M., Nimis, P.,Martin, S.,Mair, V., 2003. Mantle–crust interactions during Variscan subduction in the Eastern Alps (Nonsberg–Ulten zone): geochronology and new petrological constraints. Earth Planet. Sci. Lett. 210, 509–526.
Van Hinsbergen, D.J.J., Vissers, R.L.M., Spakman, W., 2014. Origin and consequences of Western Mediterranean subduction, rollback, and slab segmentation. Tectonics 33, 393–419.
Vanderhaeghe, O., 1999. Pervasivemelt migration from migmatites to leucogranite in the Shuswap metamorphic core complex, Canada: control of regional deformation. Tectonophysics 312, 35–55.
Vanderhaeghe, O., 2009. Migmatites, granites and orogeny: flow modes of partially molten rocks and magmas associated with melt/solid segregation in orogenic belts. Tectonophysics 477, 119–134.
Vanderhaeghe, O., 2012. The thermal–mechanical evolution of crustal orogenic belts at convergent plate boundaries: a reappraisal of the orogenic cycle. J. Geodyn. 56–57, 124–145.
Vérges, J., Fernàndez, M., 2012. Tethys-Atlantic interaction along the Iberia-Africa plate boundary: the Betic-Rif orogenic system. Tectonophysics 579, 144–172.
Vielzeuf, D., Montel, J.M., 1994. Partial melting of metagreywackes part I. Fluid-absent experiments and phase relationships. Contrib. Mineral. Petrol. 117, 375–393.
Vielzeuf, D., Clemens, J.D., Pin, C., Moinet, E., 1990. Granites, granulites and crustal differentiation. In: Vielzeuf, D., Vidal, P. (Eds.), Granulites and Crustal Evolution. Kluwer Academic Publishers, Dordrecht, pp. 59–85.
Villaros, A., Stevens, G., Buick, I.S., 2009. Tracking S-type granite from source to emplacement: Clues from garnet in the Cape Granite Suite. Lithos 112, 217–235.
von Raumer, J.F., Bussy, F., Schaltegger, U., Schulz, B., Stampfli, G.M., 2013. Pre-Mesozoic Alpine basements—their place in the European Paleozoic framework. Geol. Soc. Am. Bull. 125, 89–108.
Watson, E.B., Harrison, T.M., 1983. Zircon saturation revisited: temperature and composition effects in a variety of crustal magma types. Earth Planet. Sci. Lett. 295–304.
Watson, E.B., Wark, D.A., Thomas, J.B., 2006. Crystallization thermometers for zircon and rutile. Contrib. Mineral. Petrol. 151, 413.
Weinberg, R.F., Hasalová, P., 2015. Water-fluxed melting of the continental crust: a review. Lithos 212–215, 158–188.
White, R.W., Powell, R., 2002. Melt loss and the preservation of granulite facies mineral assemblages. J. Metamorph. Geol. 20, 621–632.
White, R.W., Powell, R., 2011. On the interpretation of retrograde reaction textures in granulite facies rocks. J. Metamorph. Geol. 29, 131–149. https://doi.org/10.1111/

j.1525-1314.2010.00905.x.
Whitehouse, M.J., Platt, J.P., 2003. Dating high-grade metamorphism - Constraints from rare-earth elements in zircon and garnet. Contrib. Mineral. Petrol. 145, 61–74.
Whitney, D.L., Evans, B.W., 2010. Abbreviations for names of Rock-Forming Minerals. Am. Mineral. 95, 185–187. https://doi.org/10.2138/am.2010.3371.
Zeck, H.P., Whitehouse, M.J., 1999. Hercynian, Pan-African, Proterozoic and Archean ionmicroprobe zircon ages for a Betic-Rif core complex, Alpine belt, W Mediterranean—Consequences for its P-T-t path. Contrib. Mineral. Petrol. 134, 134–149. https://doi.org/10.1007/s004100050474.
Zeck, H.P., Whitehouse, M.J., 2002. Repeated age resetting in zircons from Hercynian–Alpine polymetamorphic schists (Betic–Rif tectonic belt, S. Spain)—a U–Th–Pb ion microprobe study. Chem. Geol. 182, 275–292.
Zeck, H.P.,Williams, I.S., 2001. Hercynian Metamorphismin Nappe Core Complexes of the Alpine Betic–Rif Belt, Western Mediterranean—a SHRIMP Zircon Study. J. Petrol. 42, 1373–1385. https://doi.org/10.1093/petrology/42.7.1373.
Zeck, H.P., Monié, P., Villa, I.M., Hansen, B.T., 1992. Very high rates of cooling and uplift in the Alpine belt of the Betic Cordilleras, southern Spain. Geology 20, 79–82.